The Infrared Footprint Tracks of Io, Europa and Ganymede at Jupiter Observed by Juno-JIRAM

Alessandro Moirano[1], Alessandro Mura[1], Vincent Hue[2], Bertrand Bonfond[3], Linus Alexander Head[3], John E. P. Connerney[4], Alberto Adriani[5], Francesca Altieri[6], Chiara Castagnoli[1], Andrea Cicchetti[7], Bianca Maria Dinelli[8], Davide Grassi[6], Alessandra Migliorini[6], Maria L. Moriconi[9], Raffaella Noschese[7], Giuseppe Piccioni[6], Christina Plainaki[10], Pietro Scarica[6], Giuseppe Sindoni[6], Roberto Sordini[1], Federico Tosi[1], Diego Turrini[11], and Francesca Zambon[6]

[1]INAF-IAPS
[2]Aix-Marseille Université, CNRS, CNES, Institut Origines, LAM
[3]Université de Liège
[4]NASA Goddard Space Flight Center
[5]IAPS-INAF
[6]INAF
[7]Istituto Nazionale di Astrofisica
[8]Istituto di Scienza dell'Atmosfera e del Clima - CNR
[9]CNR-ISAC
[10]Agenzia Spaziale Italiana
[11]Istituto Nazionale de Astrofisica

May 13, 2023

Abstract

The electromagnetic coupling between the Galilean satellites at Jupiter and the planetary ionosphere generates an auroral footprint, whose ultimate source is the relative velocity between the moons and the corotating magnetospheric plasma. The footprint can be detected in the infrared L band (3.3-3.6 microns) by the Jovian InfraRed Auroral Mapper (JIRAM) onboard the Juno spacecraft, which can observe the footprint position with high precision. Here, we report the JIRAM data acquired since August 27th 2016 until May 23rd 2022, corresponding to the first 42 orbits of Juno. The dataset is used to compute the average position of the footprint tracks of Io, Europa and Ganymede. The result of the present analysis can help to test the reliability of magnetic field models, to calibrate ground-based observations and to highlight episodes of variability in the footprint positions, which in turn can point out specific conditions of the Jovian magnetospheric environment.

The Infrared Footprint Tracks of Io, Europa and Ganymede at Jupiter Observed by *Juno*-JIRAM

A. Moirano[1,2], A. Mura[1], V. Hue[3,4], B. Bonfond[5,6], L. A. Head[5,6], J.E.P. Connerney[7], A. Adriani[1], F. Altieri[1], C. Castagnoli[1,8,9], A. Cicchetti[1], B. M. Dinelli[8], D. Grassi[1], A. Migliorini[1], M. L. Moriconi[1], R. Noschese[1], G. Piccioni[1], C. Plainaki[10], P. Scarica[1], G. Sindoni[10], R. Sordini[1], F. Tosi[1], D. Turrini[1], F. Zambon[1]

[1]Institute for Space Astrophysics and Planetology, National Institute for Astrophysics (INAF—IAPS), Rome, Italy
[2]Sapienza University of Rome, Rome, Italy
[3]Aix-Marseille Université, CNRS, CNES, Institut Origines, LAM, Marseille, France
[4]southwest Research Institute, San Antonio, Texas, USA
[5]Laboratory for Planetary and Atmospheric Physics, Space Science, Technologies and Astrophysical Research Institute, University of Liège, Liège, Belgium
[6]Space sciences, Technologies and Astrophysics Research Institute, Université de Liège, Belgium
[7]Space Research Corporation, Annapolis, MD, USA 21403
[8]Institute of Atmospheric Sciences and Climate, National Research Council (CNR - ISAC), Bologna, Italy
[9]University of Rome Tor Vergata, Rome, Italy
[10]Italian Space Agency (ASI), Rome, Italy

Key Points:

- The position of the Io, Europa and Ganymede infrared footprints from August 2016 to May 2022 is reported, based on *Juno*-JIRAM observations.
- The average position of the three footprints is compared against magnetic field models and ultraviolet observations.
- The evidences of variations in the position of the footprints are reported and qualitatively discussed.

Corresponding author: Alessandro Moirano, `alessandro.moirano@inaf.it`

Abstract

The electromagnetic coupling between the Galilean satellites at Jupiter and the planetary ionosphere generates an auroral *footprint*, whose ultimate source is the relative velocity between the moons and the corotating magnetospheric plasma. The footprint can be detected in the infrared L band (3.3-3.6 microns) by the Jovian InfraRed Auroral Mapper (JIRAM) onboard the *Juno* spacecraft, which can observe the footprint position with high precision. Here, we report the JIRAM data acquired since August 27^{th} 2016 until May 23^{rd} 2022, corresponding to the first 42 orbits of *Juno*. The dataset is used to compute the average position of the footprint tracks of Io, Europa and Ganymede. The result of the present analysis can help to test the reliability of magnetic field models, to calibrate ground-based observations and to highlight episodes of variability in the footprint positions, which in turn can point out specific conditions of the Jovian magnetospheric environment.

Plain Language Summary

The Jovian InfraRed Auroral Mapper (JIRAM) onboard the *Juno* spacecraft around Jupiter has now been gathering six years of observations. Among the features of the Jovian aurora, here we report the position of the auroral infrared emission associated with the orbital motion of Io, Europa and Ganymede. This emission originates from the relative velocity between the moons and their surrounding magnetospheric plasma: this creates a local perturbations that travels along the magnetic field towards Jupiter's atmosphere, where emission is observed. The goal is to provide a reference track for the position of the footprints, which is then used to test the reliability of magnetic field models. Besides, by surveying over forty orbits of data, we are able to point out variations, which can suggest variable magnetospheric conditions. Lastly, the reference track can be used to improve the pointing of ground based observations of Jupiter.

1 Introduction

Jupiter hosts the most intense auroral activity in the Solar System (see review by Grodent (2015)), and its complex morphology can be observed at a variety of different wavelengths, from radio to X-ray (Drossart et al., 1989; Gladstone et al., 2002, 2007; Grodent et al., 2006; Kurth et al., 2017; Trafton et al., 1989). Among the multiple auroral features, the *satellite footprints* are emissions that can be observed at the base of the magnetic shells connected to the orbits of the Galilean moons. The footprint of Io (IFP) was the first to be observed (Clarke et al., 1996; Connerney et al., 1993; Prangé et al., 1996), followed by the Europa and Ganymede footprints (EFP and GFP, respectively) (Clarke et al., 2002) and then that of Callisto (Bhattacharyya et al., 2018). The footprints originate from the relative velocity between each moon and its surrounding plasma (Neubauer, 1980; Saur, 2004): the local perturbation at the moons excites Alfvén waves that propagates along the magnetic field lines (Acuña et al., 1981; Belcher et al., 1981; Neubauer, 1980) at a speed $v_A = B/\sqrt{\mu_0 \rho}$ (B is the magnetic field magnitude and ρ the plasma mass density). v_A is a few hundred km/s near the moons (Kivelson et al., 2004) and increases up to the speed of light in the high-latitude magnetosphere (Hinton et al., 2019). Hence, the wavefronts form a wing-shaped structure in the satellite frame, called an *Alfvén wing* (Drell et al., 1965). The Alfvén waves can exchange energy by wave-particle interaction with magnetospheric electrons (Damiano et al., 2019; Hess, Delamere, et al., 2010; Jones & Su, 2008; Sulaiman et al., 2020), which then precipitate onto the planetary ionosphere, where the footprint emission is observed (Miller et al., 2020).

In this work, we focus on the emission at the foot of the Alfvén wings, which is called the *Main Alfvén Wing* (MAW) spot (Bonfond et al., 2008). Additionally, we survey the position of the *footprint tails* downstream of the MAW spot (Bonfond et al., 2017), to be compared with the MAW spot position. The position of the MAW spot depends on

the System III longitude of the moons in Jupiter's frame (from here on, longitudes are tacitly referred in System III). Indeed, the fast Jovian rotation confines the magnetospheric plasma in a few R_J-thick disk around the *centrifugal equator*, which is located $\sim 7°$ from the rotational equators (Hill, 1979; Moirano, Gomez Casajus, et al., 2021; Phipps et al., 2020). The Galilean moons wiggle up and down in this plasmadisk as they orbit Jupiter: this affects the pattern of the Alfvén wings, thus determining the position of the MAW spot.

Since 2016, the *Juno* spacecraft has been orbiting Jupiter in a polar orbit (Bagenal et al., 2017; Connerney et al., 2017). The *Juno*-JIRAM instrument has an L-band imager designed to detect the infrared emission from the auroral H_3^+, which is produced by the reaction between the molecular hydrogen of the atmosphere and the precipitating electrons (Miller et al., 2020). The high spatial resolution of the instrument allows us to resolve the morphology of the footprints with unprecedented detail (Moirano, Mura, et al., 2021; Mura et al., 2017, 2018). Here, we report all the observations of the Io, Europa and Ganymede footprints performed by JIRAM from the first perijove (PJ) on August 27^{th} 2016 until PJ42 on May 23^{rd} 2022. At present, we find no clear evidence of the Callisto footprint in the JIRAM dataset due to the presence of the main auroral emission of Jupiter close to its expected position. Hence, Callisto will be left out of this work.

The main goal of the present work is to provide a survey of all the observations performed by *Juno*-JIRAM and the reference tracks of the Io, Europa and Ganymede infrared footprints. The results can help to test the reliability of magnetic field models by comparing JIRAM observations with their modelled position. Furthermore, the MAW spot can be a reference for calibrating ground-based observations. Lastly, the JIRAM survey can show variability in the footprints during the *Juno* mission (Moirano et al., 2023) or can be a baseline for future comparisons. As auroral emissions reflect magnetospheric processes, this evidence can highlight particular conditions within the Jovian magnetosphere.

In section 2, we introduce the JIRAM dataset and the fitting procedure used to derive the reference footprint tracks. In section 3, we show the results based on the MAW spot and the footprint-tail positions separately. In section 4, the footprint tracks are compared against the position predicted by the *Juno*-based internal magnetic field JRM33 (Connerney et al., 2022) with the external field due to the presence of the plasmadisk current Con2020 (Connerney et al., 2020; Wilson et al., 2023), as well as against the ultraviolet observations performed by the *Hubble Space Telescope* (HST) and *Juno*-UVS. In the same section, we discuss the evidence of variability in the JIRAM dataset.

2 Observations, Data Reduction and Fitting Procedure

The JIRAM L-band imager is a 128x432 pixels detector operating between 3.3-3.6 microns and with an angular resolution of about 0.01° (Adriani et al., 2017), which corresponds to a few tens of kilometers at the 1 bar level in the Jovian atmosphere (considered the "surface" of Jupiter). Due to the interference from the adjacent M-filter, an empirical background is modelled according to Mura et al. (2017) and is then subtracted from the image. This allows us to retrieve the morphology of the aurora, while slightly affecting the intensity. Nevertheless, the interference gradually conceals all the emission close to the junction between the two filters, hence the first 38 rows near the M-filter were removed.

In the present study, we survey the observations performed since PJ1 on August 27^{th} 2016 until PJ42 on May 23^{rd} 2022. To determine the position of both the MAW spots and the footprint-tail emissions, we used a 2D peak-finder routine (Natan, 2021). For the MAW spots, we gathered 259 images for Io (130 north, 129 south), 127 for Europa (54 north, 73 south) and 234 for Ganymede (95 north, 139 south). This initial dataset

was then reduced to account for batches of images that show the same MAW spot in the same sequence. Indeed, thanks to the high resolution of JIRAM, these batches do not significantly improve the determination of the footprint position with respect to a single image, but they statistically affect the result of the fitting procedure. Hence, the data points from a single sequence were binned in 500-km-wide bins, and the final dataset includes 115 data points for Io (56 north, 59 south), 55 for Europa (17 north, 38 south) and 83 for Ganymede (32 north, 51 south). To obtain the tail position, we used *sequences* - that is, tessellations of several images acquired 30 seconds apart - instead of single images. The Io footprint tail (IFPT) was observed in 170 sequences (57 north, 113 south), and the Europa and Ganymede footprint tails (EFPT and GFPT) in 58 (13 north, 45 south) and 65 (18 north, 47 south), respectively.

The coordinates of the MAW spot and the footprint-tail positions are computed at an altitude of 600±100 km above the Jovian surface, estimated by stereoscopy of PJ4 and PJ7. The positions of the two features are fitted by a Fourier expansion to determine their reference tracks. The fit is performed for each feature (MAW spot or tail) of each moon at both hemispheres separately. For each fit, the best value for the Fourier degree is estimated by computing the mean weighted sum of squared residuals (MWSSR) as function of the Fourier degree, that is:

$$MWSSR(N) = \sqrt{\frac{\sum_i W_i D_i^2}{L - (2N+1)}} \tag{1}$$

where D_i is the i-th residual (i.e: the distance between the i-th data point and the fitted curve), W_i its normalized weight, L the number of observations and N the degree of the Fourier expansion. The details of the computation of the weights in Eq.1, the uncertainty associated to the observations and the determination of the emission altitude are reported in the supporting information.

3 Results

In panel *a* and *b* of Figure 1, we report the position of the MAW spots and the footprint-tail positions respectively, alongside the results of the fitting procedure of section 2. Each point is color-coded according to its local time and two palettes were used to highlight any potential indication of local time variations. The best value for the Fourier-expansion degree N was determined to be 9 in the north and 5 in the south.

In panel *(a)* of Figure 1, in the north, only about half of each track is sampled by the JIRAM observations. JIRAM was able to observe IFP and GFP at 60°-120° and around 140° longitude respectively, while there are only a few observations for Europa around 120°. In this region, we observe deviations between the fit and JRM33+Con2020 up to ∼1000 km. Poleward deviations of about 1000 km between the GFP track and the model can also be noticed at 240°-280° longitude. In the southern hemisphere the coverage is almost complete, the largest gap being in the GFP between 0° and 40° longitude. Between 210° and 320°, the fit to the IFP, EFP and GFP are poleward of JRM33+Con2020 by up to ∼600, ∼400 and ∼200 km, respectively. Between 60° and 120° longitude, the GFP appears displaced poleward when it is observed in the dusk sector, while it is equatorward in the dawn sector. For each fit, we computed the root mean square (rms) of the residuals $R_{fit} = \sqrt{\sum_i D_i^2/L}$, which are 198, 65 and 110 km for Io, Europa and Ganymede in the north respectively, and 109, 85 and 293 km in the south.

In panel *(b)*, we report the same plots as in panel *(a)* showing the position of the footprint tails. The data coverage of the IFPT is almost complete and the only gap is around 150°-160°. This improvement is due to the long extension of the IFPT (Bonfond et al., 2017; Mura et al., 2017, 2018). All the differences between the MAW spot position and JRM33+Con2020 are also reported in the plots of panel *(b)*, as well as the transversal variability of the GFPT between 60° and 120° longitude. The rms of the residuals

R_{fit} obtained from the footprint tails are 231, 62 and 190 km for Io, Europa and Ganymede in the north respectively, and 252, 150 and 301 km in the south.

The fitted footprint tracks of panel *(a)* and *(b)* are compared in panel *(c)* and they are largely compatible within the rms of the residuals. Therefore, we suggest that both the MAW spots and the footprint tails can be used interchangeably to determine the reference ovals of the footprint tracks.

To highlight the variability of the position of the footprints, we computed the *lead angle* (Hess, Pétin, et al., 2010; Hue et al., 2023) associated with each observation. This quantity is computed by first tracing the MAW spot position along the magnetic field to the equatorial plane and then computing the angular separation with the corresponding moon at the same epoch. This quantity depends on the Alfvén travel time between the satellites and the Jovian ionosphere, so it contains information about the magnetic field and plasma mass distribution in the magnetosphere. In Figure 2, panel *(A)* and *(B)*, we report the lead angles relative to the observations of Figure 1 for the northern and southern hemisphere respectively. For each plot in both panels, the data are fitted with a periodic function $L_0 + \Delta L cos(\lambda - \phi)$, where L_0, ΔL and ϕ are free parameters and λ is the longitude of the satellites. The results of these fits are presented alongside the plots.

4 Discussion

4.1 Comparison with the JRM33+Con2020 Magnetic Field Model

We computed two predictions by expanding the spherical harmonics of JRM33 up to order 13^{th} and 18^{th}, which are the recommendations in the original work by Connerney et al. (2022), depending on the level of confidence of the magnetic field coefficients. As shown in panel *(c)* of Figure 1, the two expansions show differences in the longitude sector between 270° and 170° in the northern hemisphere. Thus, we compare the rms R_{13} and R_{18} of the distance between JIRAM data and the two JRM33+Con2020 predictions in the northern hemisphere (the two expansions lead to very similar footprint tracks in the southern hemisphere). For Io, we obtain $R_{13} = 512$ km and $R_{18} = 484$ km from the MAW spot position and $R_{13} = 424$ km and $R_{18} = 451$ km from the tail position. Indeed, in the longitude sectors 300°-330° and 100°-130°, the order 18^{th} better matches the JIRAM data, while the order 13^{th} is better between 30° and 100°. Instead, for Europa and Ganymede, R_{18} is smaller than R_{13} for both the MAW spot position and the tail positions. For Europa we obtain $R_{13} = 449$ and 549 km for the two features respectively, and $R_{18} = 320$ and 325 km, while for Ganymede $R_{13} = 609$ and 881 km, and $R_{18} = 441$ and 600 km. Therefore, we suggest expanding the JRM33 spherical harmonics up to order 18^{th} for Europa's and Ganymede's auroral emissions.

4.2 Footprint Variability: Lead Angles and Transversal Shift

The position of the MAW spots depends on the shape of the Alfvén wings, which, in turn, are determined by the magnetic field geometry and magnitude, as well as by the plasma mass density distribution in the magnetosphere. Therefore, in principle, any variation in the position of the MAW spots should be attributed to changes in either the plasma environment and/or the magnetic field. In this section, we gather the evidence of variability in the MAW spot position and we qualitatively suggest potential explanations for those observations. For this purpose, we focus on the JIRAM data acquired during different orbits but with the satellites at a similar longitude.

In the data of Figure 1 and 2, only the GFP exhibits transversal displacements. JIRAM was able to observe the GFP in both hemispheres during PJ1, PJ4, PJ7 and PJ32; among these, Ganymede orbited in the same longitude sector during both PJ1 and PJ4.

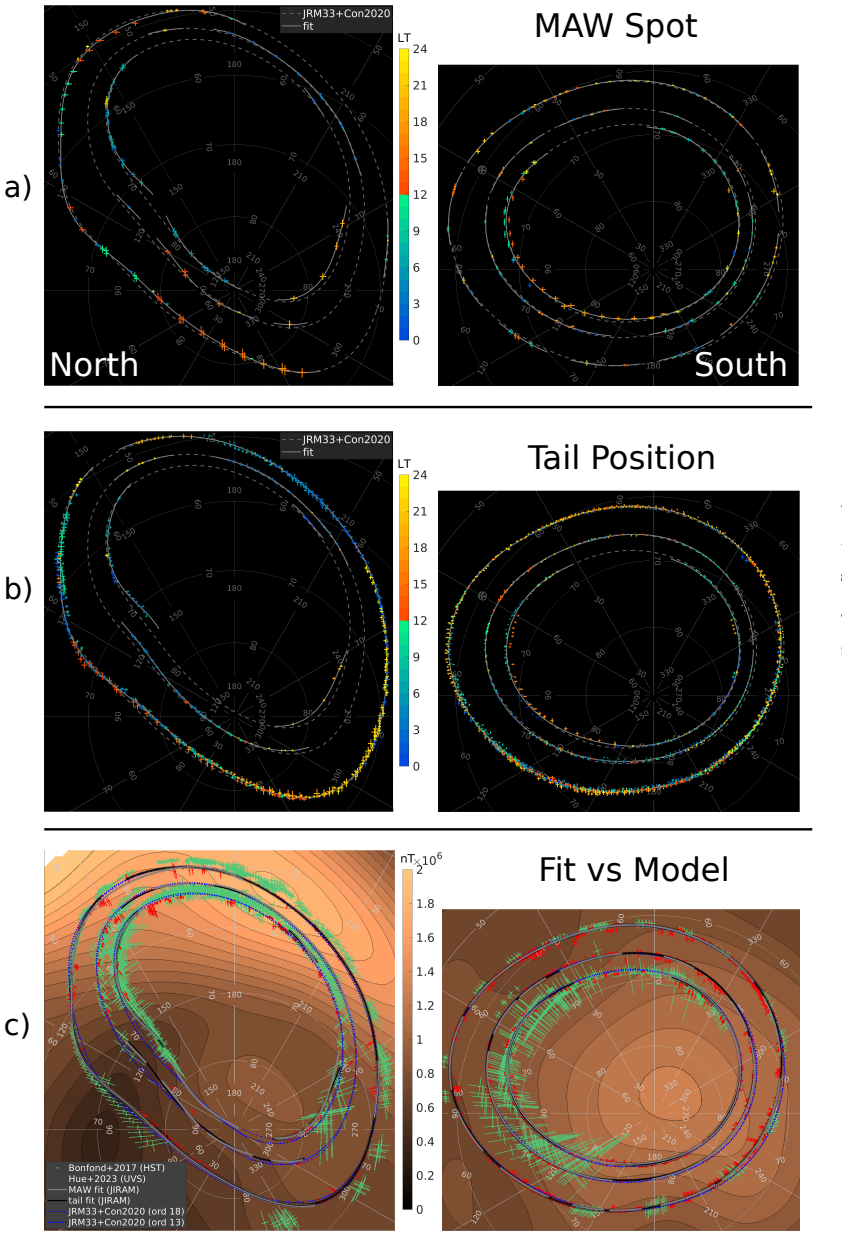

Figure 1. ***(a)*** Plot of the position of the MAW spot of Io, Europa and Ganymede in the north and south (left and right columns, respectively). The data are color-coded according to the local time of the footprint, with the cold palette for the dawn sector and the warm palette for the dusk sector. The grey continuous line is the fit to the data, the grey dashed line is the footprint track predicted by the JRM33+Con2020 magnetic field model. ***(b)*** The same as in panel *(a)*, but for the position of the footprint tails. ***(c)*** Comparison among the fits obtained from the MAW spots (grey line) and the footprint tails (black line), the JRM33+Con2020 model expanded up to order 13^{th} and 18^{th} (blue dotted and blue dashed lines, respectively) and the ultraviolet observations performed by HST (green points, from Bonfond et al. (2017)) and *Juno*-UVS (red points, from Hue et al. (2023)). The grey and black lines are surrounded by thin dotted lines of the same colors: they represent the confidence of the two fits, respectively. The background contours are the magnetic field magnitude at the surface according to JRM33+Con2020 to order 18^{th}.

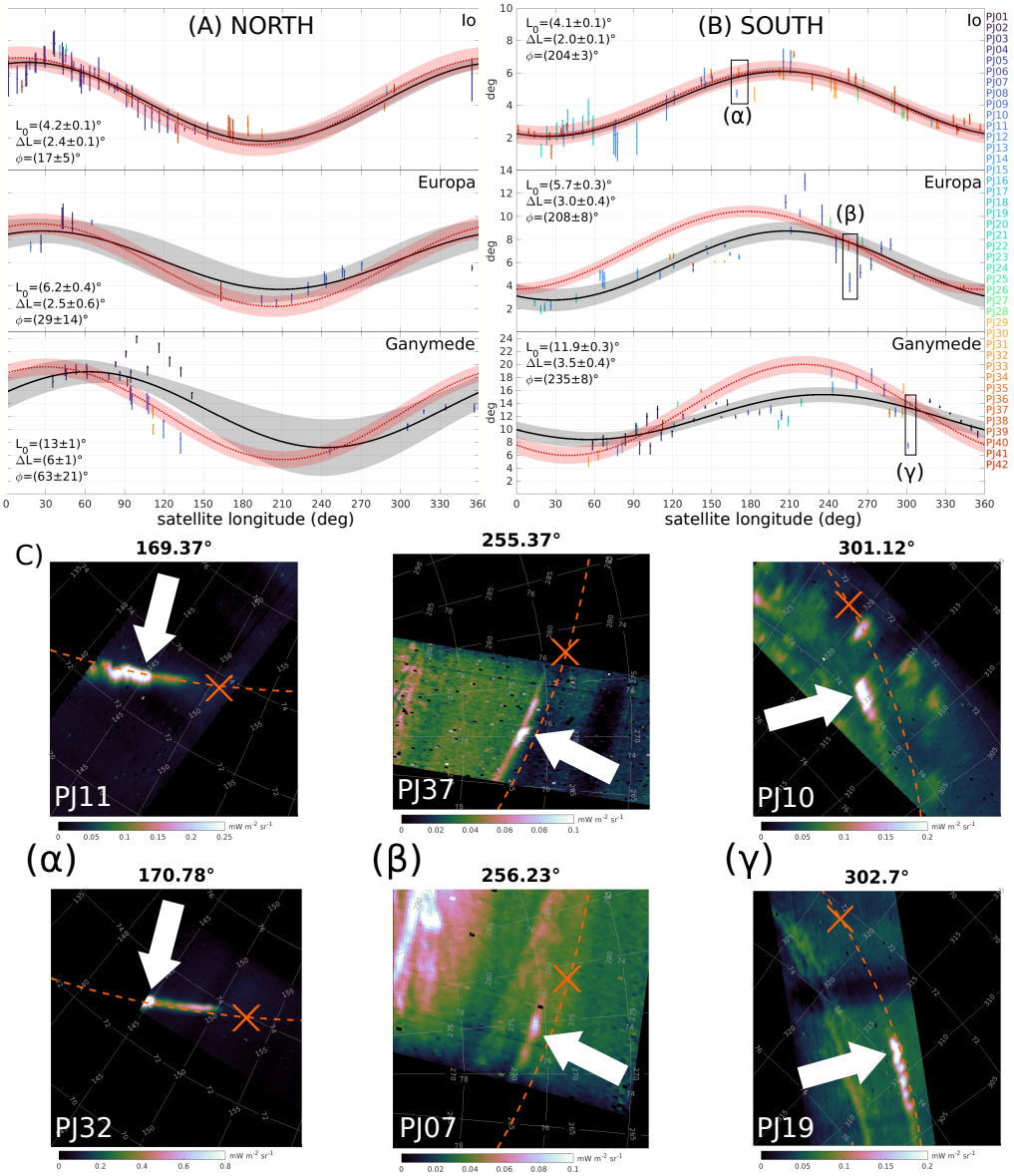

Figure 2. ***(A)***: Lead angles of the Io, Europa and Ganymede MAW spots in the northern hemisphere. The data are color-coded according the orbit number. The black line is the fit with a first-order Fourier expansion, the grey shaded area the associated 95% confidence interval. The red dotted line and the red shaded area are the fit to the lead angle derived from *Juno*-UVS observations with its uncertainty (Hue et al., 2023). In each plot, we report the parameters obtained by fitting $L_0 + \Delta Lcos(\lambda - \phi)$ to JIRAM data. ***(B)***: the same as panel *(A)*, but for the southern hemisphere. The boxes labelled α, β and γ highlight the cases of variability reported in panel *(C)*. ***(C)***: examples of variation in the MAW spot position for Io (left), Europa (center) and Ganymede (right). The orange dashed line is the satellite footprint track according to JRM33+Con2020, the cross is the magnetic footprint of each moon at the time of the acquisition of the image. The System III longitude of the satellites is reported above each image. The white arrows point to the MAW spot in each image.

The overlap of these two orbits allowed to sample the GFP track at 140° longitude and 60°-70° latitude north at two different times. No clear evidence of latitudinal displacement is observed in this region. The local time (LT) of the MAW spot observed during PJ1 and PJ4 was 4-5 hr and 7-9 hr respectively, thus both observations were in the dawn sector. In the southern hemisphere, the GFP was observed between 70° and 80° longitude during both orbits, showing a transversal displacement of 880±220 km. The LT of those observations was 11-12 hr for PJ1 (dawn sector, with the footprint equatorward displaced) and 15 hr for PJ4 (dusk sector, with the footprint poleward displaced). This suggests that the variability of the GFP position reported here might be due to a local-time asymmetry. Further evidences can be observed in the GFP and the GFPT position in the southern hemisphere at ∼165° longitude, where the emission during PJ25 (LT = 14 hr) was equatorward with respect to PJ21 (LT = 2 hr) and PJ32 (LT = 5 hr) by 370±140 km, and at 310° longitude, where the tail during PJ10 (LT = 19) was poleward with respect to PJ19 (LT = 4) and PJ33 (LT = 12 hr) by about 660±330 km. We also looked for a potential day-night correlation (not shown), but the transversal shift showed no systematic dependency with this criterion. The transversal displacement of the GFP has already been observed by HST (Grodent et al., 2008) and it have been explained by variations in the plasmadisk mass and/or radial transport (Promfu et al., 2022). Although the observations performed during PJ1 and PJ4 suggest local-time variability, we can not completely rule out a global variation of the plasmadisk. Nevertheless, this change should have occurred over less than 10 hours in order to explain the different north-south displacement observed by JIRAM. Unfortunately, JIRAM did not record the GFP crossing from the dawn to the dusk sector (or vice-versa), which might have represented stronger evidence of its local-time variability.

The lead angle shown in Figure 2 can help to detect evidence of longitudinal variability between different orbits. In the northern hemisphere (panel *(A)*), we report a single case for Io at ∼290° between PJ20 and PJ34, and one for Ganymede between 90° and 135°, where the lead angle of PJ1 was larger than the one of PJ4, PJ9, PJ32 and PJ37. In the southern hemisphere (panel *(B)*), we identified several cases that show different lead angle at the same satellite longitude: for Io there is PJ11-PJ32 at 170° longitude; for Europa PJ18-PJ32 at 120°, PJ8-PJ40 at 135°, PJ14-PJ29 at 160°, PJ7-PJ37 at 255° and PJ7-PJ26 at 265°; for Ganymede PJ1-PJ4 between 90° and 120°, PJ4-PJ7 at 160° and PJ30-PJ33 and PJ10-PJ19, both around 300°. For each satellite, we select one example pair of observations, labelled α, β and γ in panel *(B)*, and the corresponding images are reported in panel *(C)*. Case α shows the IFP during PJ11 and PJ32, with lead angles 4.7±0.2° and 6.0±0.3°, respectively. Additionally, the distance between the MAW spot and the tip of the leading spot to the right of the MAW spot, which is associated to the electron beam accelerated above the ionosphere at the opposite hemisphere (Bonfond et al., 2008; Hess, Delamere, et al., 2010), is about 1000 km and 1700 km respectively. This pair of observations was analyzed in Moirano et al. (2023), where the difference was attributed either to changes in the state of the Io Plasma Torus (Bagenal & Dols, 2020) between the two orbits or to the local-time asymmetry of the plasma torus. Case β shows the longitudinal displacement of the EFP by comparing PJ7 and PJ37, when the lead angle was 4.3±0.8° and 7.5±0.5° respectively, while Europa was at the same longitude within less than 1°. Similarly, in case γ, the GFP exhibits both transversal and longitudinal displacement by comparing PJ10 and PJ19 (lead angle 7.5±0.5° and 13.8±0.5°, respectively). Although the transversal displacement in case γ can be ascribed to a local time asymmetry as discussed in the previous paragraph, we found no clear dependency of the lead angle on the local time.

The longitudinal and the transversal displacements of the footprints can be explained by two different processes. The longitudinal displacement at a given satellite longitude can be caused by a change in the Alfvén travel time - which corresponds to a variation in the plasma environment - or to a change in the radial current of the plasmadisk - which causes an azimuthal stretch of the magnetic field lines. On the other hand, a transver-

sal displacement can be explained by the satellites connecting to different magnetic shells, which can be due to variations in the azimuthal component of the magnetodisk current that radially stretches the magnetic field. We estimated the longitudinal and transversal displacement by changing the radial current of the Con2020 model $\mu_0 I_R/2\pi$ between 7.7 and 35.2 MA, and the azimuthal current $\mu_0 I_{MD}/2$ between 124.2 and 156.1 nT, according to the *Juno* magnetometer data (Connerney et al., 2020). The longitudinal shift caused by the radial current variations is approximately 70, 200 and 450 km for Io, Europa and Ganymede respectively, while the transversal shift is about 100, 250 and 650 km. For Io and Europa, these values are similar to or smaller than the footprint size; hence it appears unlikely that the variability observed at those moons is caused by changes in the plasmadisk currents. Furthermore, both the IFP and EFP exhibited lead angle variations, but no transversal variation, which suggests variations in the plasma environment around the two satellites. On the other hand, the GFP displacement in Figure 1 may be compatible with magnetodisk variations such as the ones detected by the *Juno* magnetometer. Thus, we suggest that the variations in the GFP position can be caused either by local time asymmetry and temporal variations of the magnetodisk currents or changes in the plasmadisk mass content.

4.3 Comparison with *Juno*-UVS and HST Observations

In panel *(c)* of Figure 1, we compare the fit obtained from the MAW spot and tail positions against the ultraviolet observations performed by HST (Bonfond et al., 2017) and *Juno*-UVS (Hue et al., 2023). For the IFP in the northern hemisphere, the HST observations are systematically equatorward with respect to both the JIRAM-based fits and UVS data. The HST, JIRAM and UVS osbervations of the GFP at ∼140° longitude, 65°-80° latitude are consistent, while they are only marginally in agreement with JRM33+Con2020. In the south, the HST observations usually lie equatorward with respect to the *Juno* measurements roughly between 30° and 120° longitude, while at the other longitudes the data from the two spacecrafts agree within the HST uncertainty. The HST data of the GFP between 40° and 60° longitude seems to suggest a transversal shift of the GFP of about 2400 km between September 2009 (poleward) and December 2000, January 2001 and May 2007 (equatorward). We inspected the local-time distribution of these four set, of observations, but we found no clear evidence of local-time dependency as in the JIRAM data. Lastly, the lack of observations in the northern hemisphere during September 2009 prevents a north-south comparison of this shift.

The referencing of the HST images onto the Jovian surface is radically different from the one used for *Juno*. For HST, the inferred position of the footprints relies on the localization of the planetary center, which in turn is determined by fitting the planetary limb in the HST images themselves (Bonfond et al., 2009). On the other hand, *Juno*-based observations are localized using the spacecraft ephemeris and the instrument pointing, which are provided by the Navigation and Ancillary Information Facility (NAIF, C. H. Acton (1996); C. Acton et al. (2018)). Therefore, the different referencing procedures for HST and *Juno* might be the root cause of the discrepancy among the observations performed by the two spacecrafts. Now, thanks to the fits in Figure 1, it becomes possible to automatically compute the location of Jupiter's center relative to the IFP MAW spot for any HST image in which the Io footprint is visible and use this spot to improve significantly the referencing accuracy. This new method assumes that the location of the MAW spot is stable through time at resolution of HST and it can not be used to further study subtle variations of the MAW spot location as a function of the torus state. Nevertheless, both the data shown in Figure 1 and the Io lead angle in Figure 2 suggest that the IFP position varies only occasionally, thus we believe that its MAW spot is a reliable reference.

The *Juno*-UVS data in Figure 1 are very consistent with the JIRAM fits. The UVS observation of the IFP between 60° and 120° longitude performed during PJ8, PJ12, PJ15

and PJ18 matches very well the fits in the same region, which was observed by JIRAM during PJ4, PJ7, PJ15 and PJ18. The UV and IR measurements also agree between 250° and 290° longitude of the GFP, where they both show a poleward displacement with respect to JRM33+Con2020. UVS data shows the transversal displacement in the GFP at ∼75°-90° longitude, where the GFP was displaced poleward during PJ7 (LT = 18 hr) with respect to PJ27 (LT = 8). Unfortunately, no measurements are reported in the northern hemisphere during those PJs for comparison. In Figure 2, the lead angle derived from JIRAM data is compared with the one from UVS data. For Io, the sinusoidal fit to the lead angle appears almost symmetric between the two hemispheres, apart from a phase difference of 187±8°, and it matches the result obtained by UVS. The lead angle phases are consistent with the tilt of the centrifugal equator towards ∼200° longitude (Moirano, Gomez Casajus, et al., 2021; Phipps et al., 2020) and the consequent wiggling up and down of Io within the Io Plasma Torus. The Europa lead angle derived in the northern hemisphere is also compatible with the southern one, the phase difference between the two being ∼179±22°. The phase of the fit to the lead angle is also compatible with the position of the centrifugal equator, showing a maximum at 29±14° in the north and 208±8° in the south. The UVS results shows a larger lead angle overall, and the southern hemisphere the phase difference between JIRAM and UVS is about 20°. At Ganymede, the amplitude of the lead angle in the northern hemisphere is larger than the amplitude in the south ($\Delta L = 6\pm1°$ and 3.5±0.4°, respectively), and the two fits are out of phase by 172±29°. Unlike the Io and Europa lead angles, the Ganymede lead angle peaks at 63±21° in the north and 235±8° in the south, while UVS data reported ∼30° and ∼220°, respectively. The differences between the JIRAM and UVS lead angles at Europa and Ganymede might be due to the different coverages between the two instrument, combined with the intrinsic variability of these footprints. Despite these differences, both datasets are overall consistent with the geometry of the Jovian magnetosphere and its plasma distribution.

5 Conclusions

We reported the *Juno*-JIRAM infrared observation of the Io, Europa and Ganymede auroral footprints observed over 42 spacecraft orbits, between August 2016 and May 2022. The main goal is to provide the reference tracks for the three footprints. Further results of this work can be summarized as follow:

- The *Juno*-based magnetic field model JRM33+Con2020 (Connerney et al., 2020, 2022; Wilson et al., 2023) precisely predict the footprint tracks, although variations up to ∼1000 km are reported between 60° and 140° longitude in the northern hemisphere, as well as deviations up to ∼600km between 210° and 320° longitude in the south.
- All three footprints exhibit evidence of longitudinal variability, which can be inferred by computing their lead angles. However, only the GFP shows clear evidence of transversal variations, which appear to be local-time dependent.
- The transversal shift of the GFP might be explained by variations in the external magnetic field due to the plasmadisk current, which radially stretches the magnetic field outwards.
- The positions of the MAW spots from JIRAM agree very well with the *Juno*-UVS observations, while the positions derived from HST campaigns are occasionally systematically displaced (such as the IFP north).
- The Io lead angle derived here is in good agreement with the lead angle from *Juno*-UVS data, as well as the Europa lead angle in the northern hemisphere. Instead, amplitude and phase deviations between the two datasets are observed for the EFP in the south and for the GFP in both hemispheres.

Open Research Section

JIRAM data and materials used in this study are publicly available on the Planetary Data System (https://pds-atmospheres.nmsu.edu/data_and_services/atmospheres_data/JUNO/jiram.html). The repository for the data products used in this study is :https://doi.org/10.5281/zenodo.7924394 (Moirano, 2023).

Acknowledgments

The authors thank Agenzia Spaziale Italiana (ASI) for supporting the JIRAM contribution to the Juno mission (including this work) under the ASI contract 2016-23-H.0. This publication benefits from the support of the French Community of Belgium in the context of the FRIA Doctoral Grant awarded to L.H.

References

Acton, C., Bachman, N., Semenov, B., & Wright, E. (2018, January). A look towards the future in the handling of space science mission geometry. *Planetary and Space Science*, *150*, 9–12. doi: 10.1016/j.pss.2017.02.013

Acton, C. H. (1996, January). Ancillary data services of NASA's Navigation and Ancillary Information Facility. *Planetary and Space Science*, *44*(1), 65–70. doi: 10.1016/0032-0633(95)00107-7

Acuña, M. H., Neubauer, F. M., & Ness, N. F. (1981, September). Standing Alfvén wave current system at Io: Voyager 1 observations. *J. Geophys. Res.*, *86*(A10), 8513–8521. doi: 10.1029/JA086iA10p08513

Adriani, A., Filacchione, G., Di Iorio, T., Turrini, D., Noschese, R., Cicchetti, A., ... Olivieri, A. (2017, November). JIRAM, the Jovian Infrared Auroral Mapper. *Space Sci Rev*, *213*(1-4), 393–446. doi: 10.1007/s11214-014-0094-y

Bagenal, F., Adriani, A., Allegrini, F., Bolton, S. J., Bonfond, B., Bunce, E. J., ... Zarka, P. (2017, November). Magnetospheric Science Objectives of the Juno Mission. *Space Sci Rev*, *213*(1-4), 219–287. doi: 10.1007/s11214-014-0036-8

Bagenal, F., & Dols, V. (2020, May). The Space Environment of Io and Europa. *J. Geophys. Res. Space Physics*, *125*(5). doi: 10.1029/2019JA027485

Belcher, J. W., Goertz, C. K., Sullivan, J. D., & Acuña, M. H. (1981). Plasma observations of the Alfvén wave generated by Io. *Journal of Geophysical Research: Space Physics*, *86*(A10), 8508–8512. doi: 10.1029/JA086iA10p08508

Bhattacharyya, D., Clarke, J. T., Montgomery, J., Bonfond, B., Gérard, J., & Grodent, D. (2018, January). Evidence for Auroral Emissions From Callisto's Footprint in HST UV Images. *J. Geophys. Res. Space Physics*, *123*(1), 364–373. doi: 10.1002/2017JA024791

Bonfond, B., Grodent, D., Gérard, J.-C., Radioti, A., Dols, V., Delamere, P. A., & Clarke, J. T. (2009, July). The Io UV footprint: Location, inter-spot distances and tail vertical extent. *J. Geophys. Res.*, *114*(A7), n/a–n/a. doi: 10.1029/2009JA014312

Bonfond, B., Grodent, D., Gérard, J.-C., Radioti, A., Saur, J., & Jacobsen, S. (2008, March). UV Io footprint leading spot: A key feature for understanding the UV Io footprint multiplicity? *Geophys. Res. Lett.*, *35*(5), L05107. doi: 10.1029/2007GL032418

Bonfond, B., Saur, J., Grodent, D., Badman, S. V., Bisikalo, D., Shematovich, V., ... Radioti, A. (2017, August). The tails of the satellite auroral footprints at Jupiter. *J. Geophys. Res. Space Physics*, *122*(8), 7985–7996. doi: 10.1002/2017JA024370

Clarke, J. T., Ajello, J., Ballester, G., Ben Jaffel, L., Connerney, J., Gérard, J.-C., ... Waite, J. H. (2002, February). Ultraviolet emissions from the magnetic footprints of Io, Ganymede and Europa on Jupiter. *Nature*, *415*(6875), 997–1000. doi: 10.1038/415997a

Clarke, J. T., Ballester, G. E., Trauger, J., Evans, R., Connerney, J. E. P., Stapelfeldt, K., ... Westphal, J. A. (1996, October). Far-Ultraviolet Imaging of Jupiter's Aurora and the Io "Footprint". *Science*, *274*(5286), 404–409. doi: 10.1126/science.274.5286.404

Connerney, J. E. P., Adriani, A., Allegrini, F., Bagenal, F., Bolton, S. J., Bonfond, B., ... Waite, J. (2017, May). Jupiter's magnetosphere and aurorae observed by the Juno spacecraft during its first polar orbits. *Science*, *356*(6340), 826–832. doi: 10.1126/science.aam5928

Connerney, J. E. P., Baron, R., Satoh, T., & Owen, T. (1993, November). Images of Excited H3+ at the Foot of the Io Flux Tube in Jupiter's Atmosphere. *Science*, *262*(5136), 1035–1038. doi: 10.1126/science.262.5136.1035

Connerney, J. E. P., Timmins, S., Herceg, M., & Joergensen, J. L. (2020). A Jovian Magnetodisc Model for the Juno Era. *Journal of Geophysical Research: Space Physics*, *125*(10), e2020JA028138. doi: 10.1029/2020JA028138

Connerney, J. E. P., Timmins, S., Oliversen, R. J., Espley, J. R., Joergensen, J. L., Kotsiaros, S., ... Levin, S. M. (2022). A New Model of Jupiter's Magnetic Field at the Completion of Juno's Prime Mission. *Journal of Geophysical Research: Planets*, *127*(2), e2021JE007055. doi: 10.1029/2021JE007055

Damiano, P. A., Delamere, P. A., Stauffer, B., Ng, C.-S., & Johnson, J. R. (2019). Kinetic Simulations of Electron Acceleration by Dispersive Scale Alfvén Waves in Jupiter's Magnetosphere. *Geophysical Research Letters*, *46*(6), 3043–3051. doi: 10.1029/2018GL081219

Drell, S. D., Foley, H. M., & Ruderman, M. A. (1965, February). Drag and Propulsion of Large Satellites in the Ionosphere; An Alfv\'en Propulsion Engine in Space. *Physical Review Letters*, *14*(6), 171–175. doi: 10.1103/PhysRevLett.14.171

Drossart, P., Maillard, J., Caldwell, J., Kim, S., Watson, J., Majewski, W., ... Wagener, R. (1989, August). Detection of H3+ on Jupiter. *Nature*, *340*. doi: 10.1038/340539a0

Gladstone, G. R., Stern, S. A., Slater, D. C., Versteeg, M., Davis, M. W., Retherford, K. D., ... Nichols, J. D. (2007, October). Jupiter's Nightside Airglow and Aurora. *Science*, *318*(5848), 229–231. doi: 10.1126/science.1147613

Gladstone, G. R., Waite, J. H., Grodent, D., Lewis, W. S., Crary, F. J., Elsner, R. F., ... Cravens, T. E. (2002, February). A pulsating auroral X-ray hot spot on Jupiter. *Nature*, *415*(6875), 1000–1003. doi: 10.1038/4151000a

Grodent, D. (2015, April). A Brief Review of Ultraviolet Auroral Emissions on Giant Planets. *Space Sci Rev*, *187*(1-4), 23–50. doi: 10.1007/s11214-014-0052-8

Grodent, D., Gérard, J.-C., Gustin, J., Mauk, B. H., Connerney, J. E. P., & Clarke, J. T. (2006). Europa's FUV auroral tail on Jupiter. *Geophysical Research Letters*, *33*(6). doi: https://doi.org/10.1029/2005GL025487

Grodent, D., Gérard, J.-C., Radioti, A., Bonfond, B., & Saglam, A. (2008). Jupiter's changing auroral location. *Journal of Geophysical Research: Space Physics*, *113*(A1). doi: 10.1029/2007JA012601

Hess, S. L. G., Delamere, P., Dols, V., Bonfond, B., & Swift, D. (2010, June). Power transmission and particle acceleration along the Io flux tube. *J. Geophys. Res.*, *115*(A6), n/a–n/a. doi: 10.1029/2009JA014928

Hess, S. L. G., Pétin, A., Zarka, P., Bonfond, B., & Cecconi, B. (2010, August). Lead angles and emitting electron energies of Io-controlled decameter radio arcs. *Planetary and Space Science*, *58*(10), 1188–1198. doi: 10.1016/j.pss.2010.04.011

Hill, T. (1979). Inertial limit on corotation. *J. Geophys. Res.*, *84*(A11), 6554. doi: 10.1029/JA084iA11p06554

Hinton, P. C., Bagenal, F., & Bonfond, B. (2019). Alfvén Wave Propagation in the Io Plasma Torus. *Geophysical Research Letters*, *46*(3), 1242–1249. doi: 10.1029/2018GL081472

Hue, V., Gladstone, G. R., Louis, C. K., Greathouse, T. K., Bonfond, B., Szalay, J. R., ... Connerney, J. (2023). The Io, Europa and Ganymede auroral footprints at Jupiter in the ultraviolet: Positions and equatorial lead angles. *Journal of Geophysical Research: Space Physics*, *n/a*(n/a), e2023JA031363. doi: 10.1029/2023JA031363

Jones, S. T., & Su, Y.-J. (2008). Role of dispersive Alfvén waves in generating parallel electric fields along the Io-Jupiter fluxtube. *Journal of Geophysical Research: Space Physics*, *113*(A12). doi: https://doi.org/10.1029/2008JA013512

Kivelson, M. G., Bagenal, F., Kurth, W. S., Neubauer, F. M., Paranicas, C., & Saur, J. (2004). Magnetospheric Interactions with Satellites. In *Jupiter: The Planet, Satellites and Magnetosphere* (F. Bagenal ed., Vol. 21, p. 513). Cambridge UK: Cambridge Univ. Press.

Kurth, W. S., Imai, M., Hospodarsky, G. B., Gurnett, D. A., Louarn, P., Valek, P., ... Zarka, P. (2017). A new view of Jupiter's auroral radio spectrum. *Geophysical Research Letters*, *44*(14), 7114–7121. doi: 10.1002/2017GL072889

Miller, S., Tennyson, J., Geballe, T. R., & Stallard, T. (2020, August). Thirty years of H 3 + astronomy. *Rev. Mod. Phys.*, *92*(3), 035003. doi: 10.1103/RevModPhys.92.035003

Moirano, A. (2023, May). *Data for the research article: "The Infrared Footprint Tracks of Io, Europa and Ganymede at Jupiter Observed by Juno-JIRAM".* Zenodo. doi: 10.5281/zenodo.7924394

Moirano, A., Gomez Casajus, L., Zannoni, M., Durante, D., & Tortora, P. (2021). Morphology of the Io Plasma Torus From Juno Radio Occultations. *Journal of Geophysical Research: Space Physics*, *126*(10), e2021JA029190. doi: 10.1029/2021JA029190

Moirano, A., Mura, A., Adriani, A., Dols, V., Bonfond, B., Waite, J. H., ... Bolton, S. J. (2021). Morphology of the Auroral Tail of Io, Europa, and Ganymede From JIRAM L-Band Imager. *Journal of Geophysical Research: Space Physics*, *126*(9), e2021JA029450. doi: 10.1029/2021JA029450

Moirano, A., Mura, A., Bonfond, B., Connerney, J., Dols, V., Grodent, D., ... Zambon, F. (2023). Manuscript #2023JA031288 Variability of the Auroral Footprint of Io Detected by Juno-JIRAM and Modelling of the Io Plasma Torus. *Journal of Geophysical Research: Space Physics*.

Mura, A., Adriani, A., Altieri, F., Connerney, J. E. P., Bolton, S. J., Moriconi, M. L., ... Olivieri, A. (2017, June). Infrared observations of Jovian aurora from Juno's first orbits: Main oval and satellite footprints: Jovian Aurora IR Observations From Juno. *Geophys. Res. Lett.*, *44*(11), 5308–5316. doi: 10.1002/2017GL072954

Mura, A., Adriani, A., Connerney, J. E. P., Bolton, S., Altieri, F., Bagenal, F., ... Turrini, D. (2018, August). Juno observations of spot structures and a split tail in Io-induced aurorae on Jupiter. *Science*, *361*(6404), 774–777. doi: 10.1126/science.aat1450

Natan, A. (2021). *Fast 2D Peak Finder.*

Neubauer, F. (1980, March). Nonlinear standing Alfvén wave current system at Io: Theory. *J. Geophys. Res.*, *85*(A3), 1171–1178. doi: 10.1029/JA085iA03p01171

Phipps, P. H., Withers, P., Vogt, M. F., Buccino, D. R., Yang, Y., Parisi, M., ... Bolton, S. (2020, August). Where Is the Io Plasma Torus? A Comparison of Observations by Juno Radio Occultations to Predictions From Jovian Magnetic Field Models. *J. Geophys. Res. Space Physics*, *125*(8). doi: 10.1029/2019JA027633

Prangé, R., Rego, D., Southwood, D., Zarka, P., Miller, S., & Ip, W. (1996, January). Rapid energy dissipation and variability of the lo–Jupiter electrodynamic circuit. *Nature*, *379*(6563), 323–325. doi: 10.1038/379323a0

Promfu, T., Nichols, J. D., Wannawichian, S., Clarke, J. T., Vogt, M. F., & Bon-

fond, B. (2022). Ganymede's Auroral Footprint Latitude: Comparison With Magnetodisc Model. *Journal of Geophysical Research: Space Physics*, *127*(12), e2022JA030712. doi: 10.1029/2022JA030712

Saur, J. (2004). A model of Io's local electric field for a combined Alfvénic and unipolar inductor far-field coupling. *Journal of Geophysical Research: Space Physics*, *109*(A1). doi: 10.1029/2002JA009354

Sulaiman, A. H., Hospodarsky, G. B., Elliott, S. S., Kurth, W. S., Gurnett, D. A., Imai, M., ... Bolton, S. J. (2020, August). Wave-particle interactions associated with Io's auroral footprint: Evidence of Alfvén, ion cyclotron, and whistler modes. *Geophys. Res. Lett.*. doi: 10.1029/2020GL088432

Trafton, L., Carr, J., Lester, D., & Harvey, P. (1989). Jupiter's Aurora: Detection of Quadrupole h2 Emission. *NASA Special Publication*, *494*.

Wilson, R. J., Vogt, M. F., Provan, G., Kamran, A., James, M. K., Brennan, M., & Cowley, S. W. H. (2023, February). Internal and External Jovian Magnetic Fields: Community Code to Serve the Magnetospheres of the Outer Planets Community. *Space Science Reviews*, *219*(1), 15. doi: 10.1007/s11214-023-00961-3

Figure 1.

a)

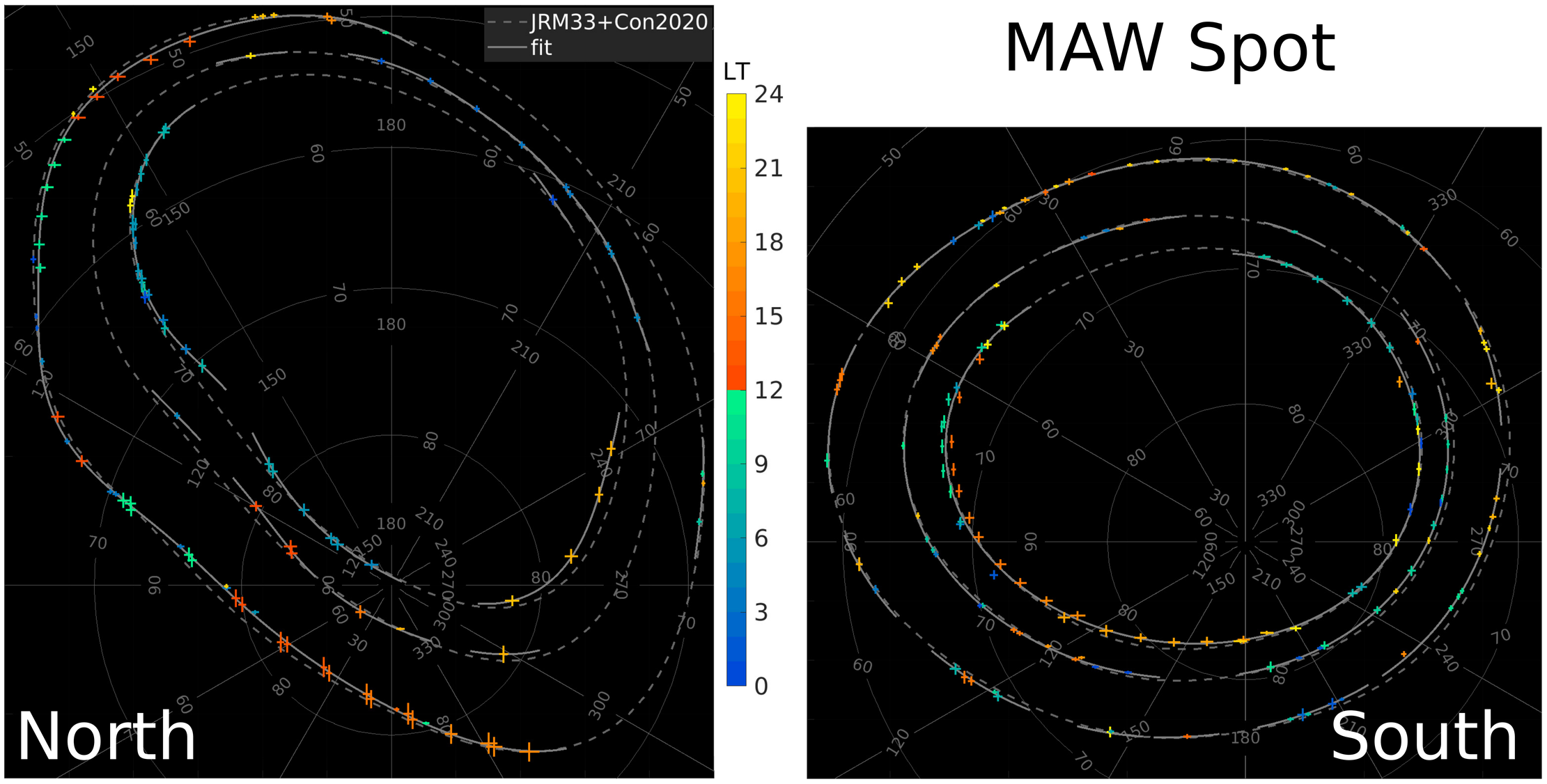

MAW Spot

b)

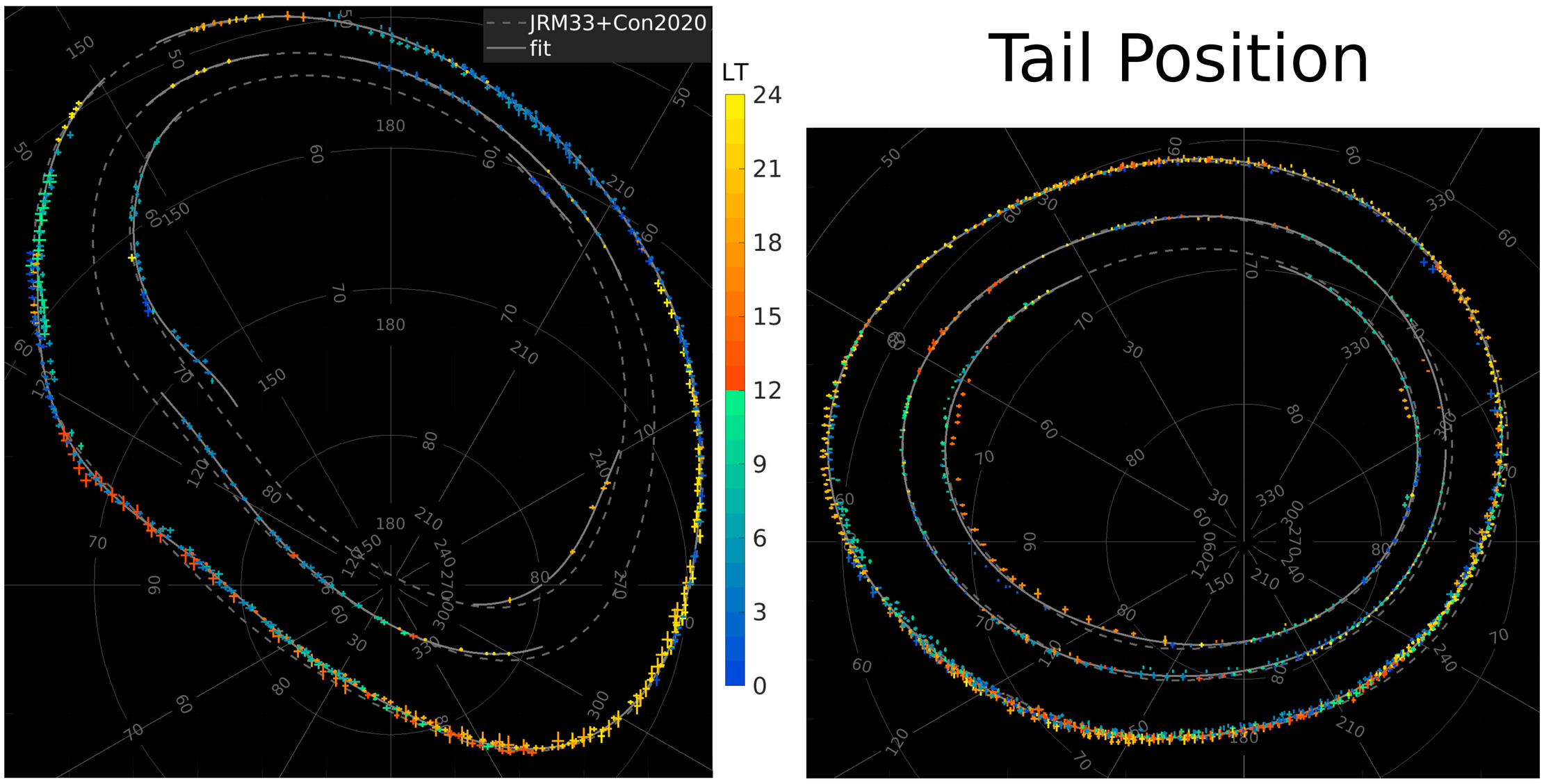

Tail Position

c)

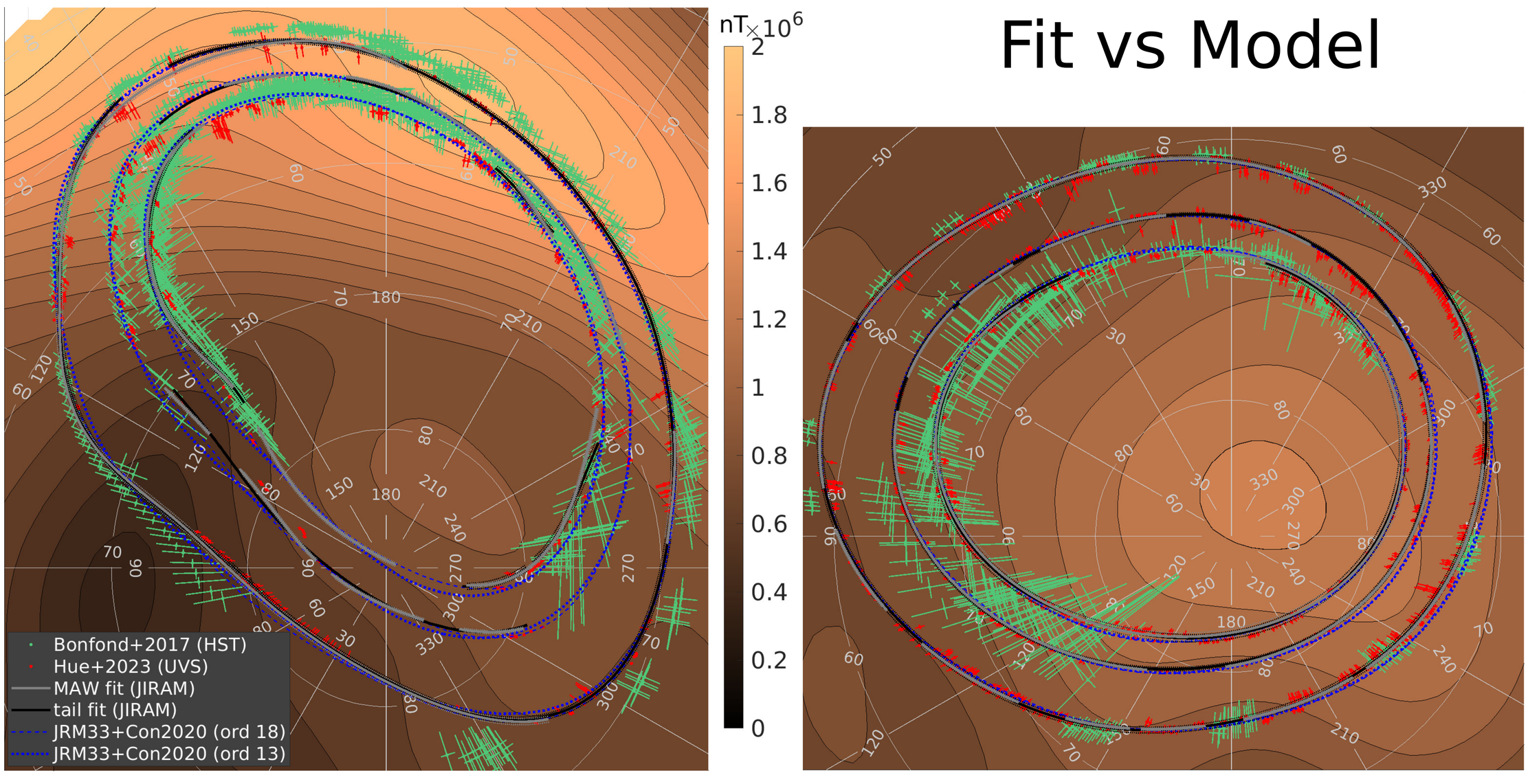

Fit vs Model

Figure 2.

(A) NORTH

Io
L_0=(4.2±0.1)°
ΔL=(2.4±0.1)°
ϕ=(17±5)°

Europa
L_0=(6.2±0.4)°
ΔL=(2.5±0.6)°
ϕ=(29±14)°

Ganymede
L_0=(13±1)°
ΔL=(6±1)°
ϕ=(63±21)°

(B) SOUTH

Io
L_0=(4.1±0.1)°
ΔL=(2.0±0.1)°
ϕ=(204±3)°
(α)

Europa
L_0=(5.7±0.3)°
ΔL=(3.0±0.4)°
ϕ=(208±8)°
(β)

Ganymede
L_0=(11.9±0.3)°
ΔL=(3.5±0.4)°
ϕ=(235±8)°
(γ)

deg

PJ01 PJ02 PJ03 PJ04 PJ05 PJ06 PJ07 PJ08 PJ09 PJ10 PJ11 PJ12 PJ13 PJ14 PJ15 PJ16 PJ17 PJ18 PJ19 PJ20 PJ21 PJ22 PJ23 PJ24 PJ25 PJ26 PJ27 PJ28 PJ29 PJ30 PJ31 PJ32 PJ33 PJ34 PJ35 PJ36 PJ37 PJ38 PJ39 PJ40 PJ41 PJ42

satellite longitude (deg)

C)

169.37°

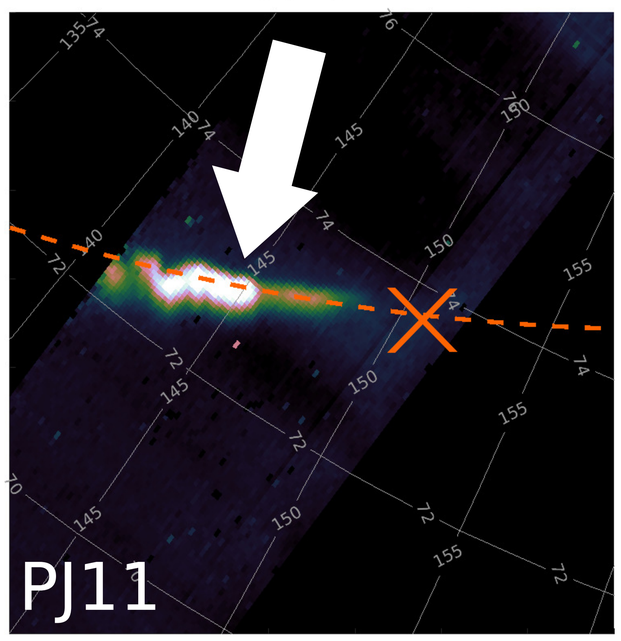

mW m^{-2} sr^{-1}
0 0.05 0.1 0.15 0.2 0.25

255.37°

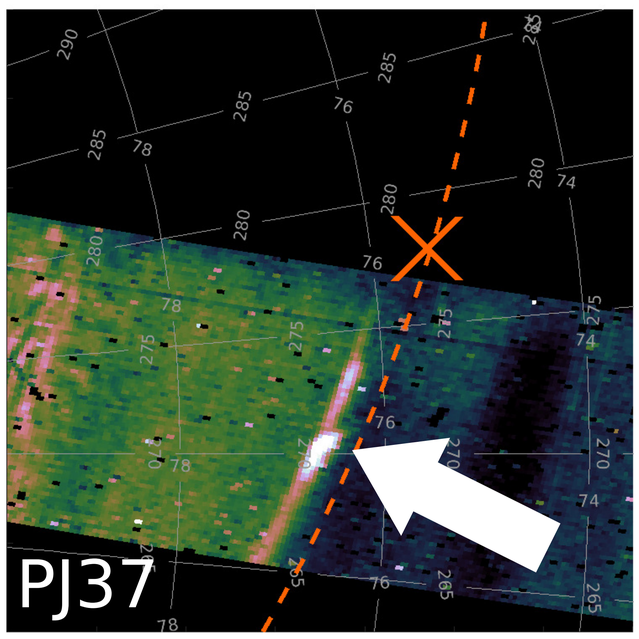

mW m^{-2} sr^{-1}
0 0.02 0.04 0.06 0.08 0.1

301.12°

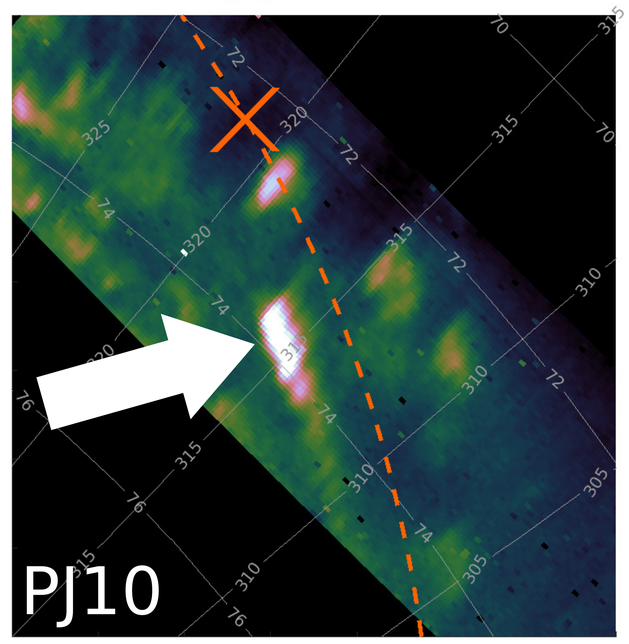

mW m^{-2} sr^{-1}
0 0.05 0.1 0.15 0.2

(α)

170.78°

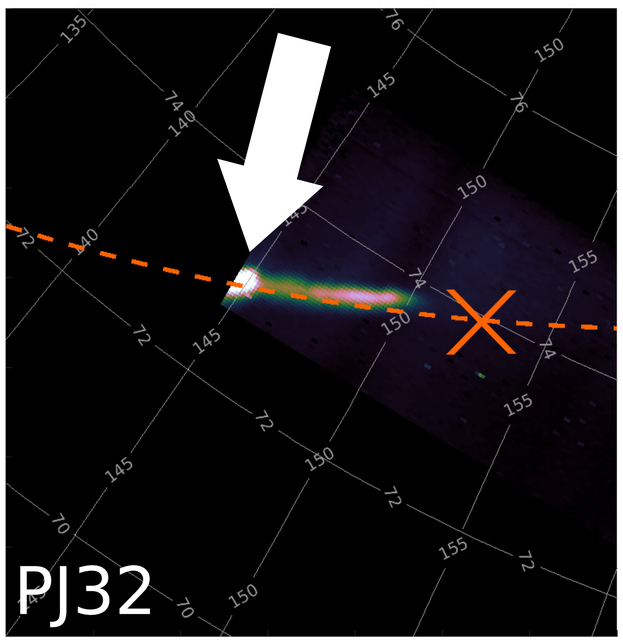

mW m^{-2} sr^{-1}
0 0.2 0.4 0.6 0.8

(β)

256.23°

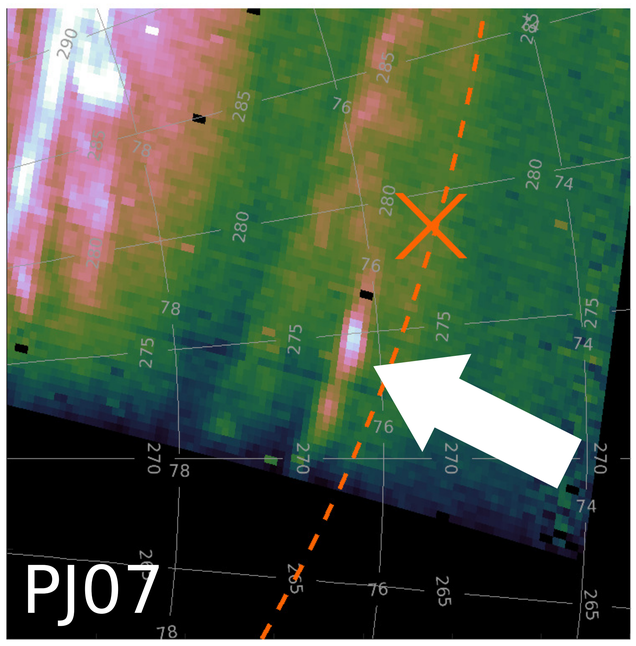

mW m^{-2} sr^{-1}
0 0.02 0.04 0.06 0.08 0.1

(γ)

302.7°

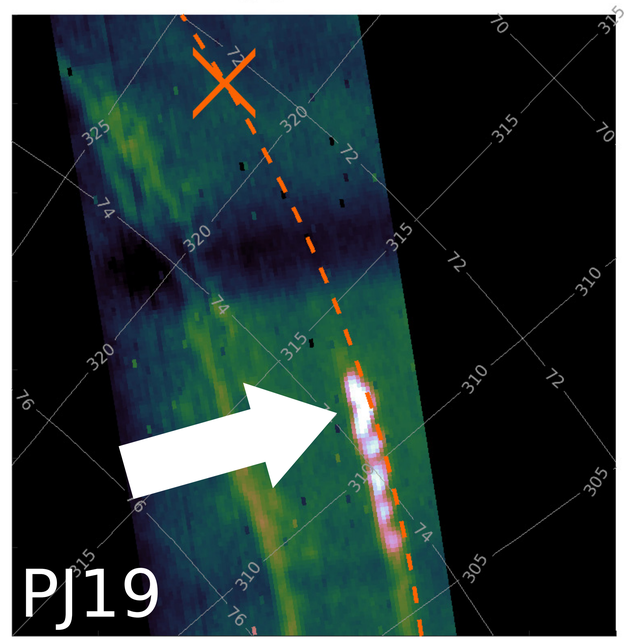

mW m^{-2} sr^{-1}
0 0.05 0.1 0.15 0.2

The Infrared Footprint Tracks of Io, Europa and Ganymede at Jupiter Observed by *Juno*-JIRAM

A. Moirano[1,2], A. Mura[1], V. Hue[3,4], B. Bonfond[5,6], L. A. Head[5,6], J.E.P. Connerney[7], A. Adriani[1], F. Altieri[1], C. Castagnoli[1,8,9], A. Cicchetti[1], B. M. Dinelli[8], D. Grassi[1], A. Migliorini[1], M. L. Moriconi[1], R. Noschese[1], G. Piccioni[1], C. Plainaki[10], P. Scarica[1], G. Sindoni[10], R. Sordini[1], F. Tosi[1], D. Turrini[1], F. Zambon[1]

[1]Institute for Space Astrophysics and Planetology, National Institute for Astrophysics (INAF—IAPS), Rome, Italy
[2]Sapienza University of Rome, Rome, Italy
[3]Aix-Marseille Université, CNRS, CNES, Institut Origines, LAM, Marseille, France
[4]southwest Research Institute, San Antonio, Texas, USA
[5]Laboratory for Planetary and Atmospheric Physics, Space Science, Technologies and Astrophysical Research Institute, University of Liège, Liège, Belgium
[6]Space sciences, Technologies and Astrophysics Research Institute, Université de Liège, Belgium
[7]Space Research Corporation, Annapolis, MD, USA 21403
[8]Institute of Atmospheric Sciences and Climate, National Research Council (CNR - ISAC), Bologna, Italy
[9]University of Rome Tor Vergata, Rome, Italy
[10]Italian Space Agency (ASI), Rome, Italy

Key Points:

- The position of the Io, Europa and Ganymede infrared footprints from August 2016 to May 2022 is reported, based on *Juno*-JIRAM observations.
- The average position of the three footprints is compared against magnetic field models and ultraviolet observations.
- The evidences of variations in the position of the footprints are reported and qualitatively discussed.

Corresponding author: Alessandro Moirano, `alessandro.moirano@inaf.it`

Abstract

The electromagnetic coupling between the Galilean satellites at Jupiter and the planetary ionosphere generates an auroral *footprint*, whose ultimate source is the relative velocity between the moons and the corotating magnetospheric plasma. The footprint can be detected in the infrared L band (3.3-3.6 microns) by the Jovian InfraRed Auroral Mapper (JIRAM) onboard the *Juno* spacecraft, which can observe the footprint position with high precision. Here, we report the JIRAM data acquired since August 27^{th} 2016 until May 23^{rd} 2022, corresponding to the first 42 orbits of *Juno*. The dataset is used to compute the average position of the footprint tracks of Io, Europa and Ganymede. The result of the present analysis can help to test the reliability of magnetic field models, to calibrate ground-based observations and to highlight episodes of variability in the footprint positions, which in turn can point out specific conditions of the Jovian magnetospheric environment.

Plain Language Summary

The Jovian InfraRed Auroral Mapper (JIRAM) onboard the *Juno* spacecraft around Jupiter has now been gathering six years of observations. Among the features of the Jovian aurora, here we report the position of the auroral infrared emission associated with the orbital motion of Io, Europa and Ganymede. This emission originates from the relative velocity between the moons and their surrounding magnetospheric plasma: this creates a local perturbations that travels along the magnetic field towards Jupiter's atmosphere, where emission is observed. The goal is to provide a reference track for the position of the footprints, which is then used to test the reliability of magnetic field models. Besides, by surveying over forty orbits of data, we are able to point out variations, which can suggest variable magnetospheric conditions. Lastly, the reference track can be used to improve the pointing of ground based observations of Jupiter.

1 Introduction

Jupiter hosts the most intense auroral activity in the Solar System (see review by Grodent (2015)), and its complex morphology can be observed at a variety of different wavelengths, from radio to X-ray (Drossart et al., 1989; Gladstone et al., 2002, 2007; Grodent et al., 2006; Kurth et al., 2017; Trafton et al., 1989). Among the multiple auroral features, the *satellite footprints* are emissions that can be observed at the base of the magnetic shells connected to the orbits of the Galilean moons. The footprint of Io (IFP) was the first to be observed (Clarke et al., 1996; Connerney et al., 1993; Prangé et al., 1996), followed by the Europa and Ganymede footprints (EFP and GFP, respectively) (Clarke et al., 2002) and then that of Callisto (Bhattacharyya et al., 2018). The footprints originate from the relative velocity between each moon and its surrounding plasma (Neubauer, 1980; Saur, 2004): the local perturbation at the moons excites Alfvén waves that propagates along the magnetic field lines (Acuña et al., 1981; Belcher et al., 1981; Neubauer, 1980) at a speed $v_A = B/\sqrt{\mu_0 \rho}$ (B is the magnetic field magnitude and ρ the plasma mass density). v_A is a few hundred km/s near the moons (Kivelson et al., 2004) and increases up to the speed of light in the high-latitude magnetosphere (Hinton et al., 2019). Hence, the wavefronts form a wing-shaped structure in the satellite frame, called an *Alfvén wing* (Drell et al., 1965). The Alfvén waves can exchange energy by wave-particle interaction with magnetospheric electrons (Damiano et al., 2019; Hess, Delamere, et al., 2010; Jones & Su, 2008; Sulaiman et al., 2020), which then precipitate onto the planetary ionosphere, where the footprint emission is observed (Miller et al., 2020).

In this work, we focus on the emission at the foot of the Alfvén wings, which is called the *Main Alfvén Wing* (MAW) spot (Bonfond et al., 2008). Additionally, we survey the position of the *footprint tails* downstream of the MAW spot (Bonfond et al., 2017), to be compared with the MAW spot position. The position of the MAW spot depends on

the System III longitude of the moons in Jupiter's frame (from here on, longitudes are tacitly referred in System III). Indeed, the fast Jovian rotation confines the magnetospheric plasma in a few R_J-thick disk around the *centrifugal equator*, which is located $\sim 7°$ from the rotational equators (Hill, 1979; Moirano, Gomez Casajus, et al., 2021; Phipps et al., 2020). The Galilean moons wiggle up and down in this plasmadisk as they orbit Jupiter: this affects the pattern of the Alfvén wings, thus determining the position of the MAW spot.

Since 2016, the *Juno* spacecraft has been orbiting Jupiter in a polar orbit (Bagenal et al., 2017; Connerney et al., 2017). The *Juno*-JIRAM instrument has an L-band imager designed to detect the infrared emission from the auroral H_3^+, which is produced by the reaction between the molecular hydrogen of the atmosphere and the precipitating electrons (Miller et al., 2020). The high spatial resolution of the instrument allows us to resolve the morphology of the footprints with unprecedented detail (Moirano, Mura, et al., 2021; Mura et al., 2017, 2018). Here, we report all the observations of the Io, Europa and Ganymede footprints performed by JIRAM from the first perijove (PJ) on August 27^{th} 2016 until PJ42 on May 23^{rd} 2022. At present, we find no clear evidence of the Callisto footprint in the JIRAM dataset due to the presence of the main auroral emission of Jupiter close to its expected position. Hence, Callisto will be left out of this work.

The main goal of the present work is to provide a survey of all the observations performed by *Juno*-JIRAM and the reference tracks of the Io, Europa and Ganymede infrared footprints. The results can help to test the reliability of magnetic field models by comparing JIRAM observations with their modelled position. Furthermore, the MAW spot can be a reference for calibrating ground-based observations. Lastly, the JIRAM survey can show variability in the footprints during the *Juno* mission (Moirano et al., 2023) or can be a baseline for future comparisons. As auroral emissions reflect magnetospheric processes, this evidence can highlight particular conditions within the Jovian magnetosphere.

In section 2, we introduce the JIRAM dataset and the fitting procedure used to derive the reference footprint tracks. In section 3, we show the results based on the MAW spot and the footprint-tail positions separately. In section 4, the footprint tracks are compared against the position predicted by the *Juno*-based internal magnetic field JRM33 (Connerney et al., 2022) with the external field due to the presence of the plasmadisk current Con2020 (Connerney et al., 2020; Wilson et al., 2023), as well as against the ultraviolet observations performed by the *Hubble Space Telescope* (HST) and *Juno*-UVS. In the same section, we discuss the evidence of variability in the JIRAM dataset.

2 Observations, Data Reduction and Fitting Procedure

The JIRAM L-band imager is a 128x432 pixels detector operating between 3.3-3.6 microns and with an angular resolution of about 0.01° (Adriani et al., 2017), which corresponds to a few tens of kilometers at the 1 bar level in the Jovian atmosphere (considered the "surface" of Jupiter). Due to the interference from the adjacent M-filter, an empirical background is modelled according to Mura et al. (2017) and is then subtracted from the image. This allows us to retrieve the morphology of the aurora, while slightly affecting the intensity. Nevertheless, the interference gradually conceals all the emission close to the junction between the two filters, hence the first 38 rows near the M-filter were removed.

In the present study, we survey the observations performed since PJ1 on August 27^{th} 2016 until PJ42 on May 23^{rd} 2022. To determine the position of both the MAW spots and the footprint-tail emissions, we used a 2D peak-finder routine (Natan, 2021). For the MAW spots, we gathered 259 images for Io (130 north, 129 south), 127 for Europa (54 north, 73 south) and 234 for Ganymede (95 north, 139 south). This initial dataset

was then reduced to account for batches of images that show the same MAW spot in the same sequence. Indeed, thanks to the high resolution of JIRAM, these batches do not significantly improve the determination of the footprint position with respect to a single image, but they statistically affect the result of the fitting procedure. Hence, the data points from a single sequence were binned in 500-km-wide bins, and the final dataset includes 115 data points for Io (56 north, 59 south), 55 for Europa (17 north, 38 south) and 83 for Ganymede (32 north, 51 south). To obtain the tail position, we used *sequences* - that is, tessellations of several images acquired 30 seconds apart - instead of single images. The Io footprint tail (IFPT) was observed in 170 sequences (57 north, 113 south), and the Europa and Ganymede footprint tails (EFPT and GFPT) in 58 (13 north, 45 south) and 65 (18 north, 47 south), respectively.

The coordinates of the MAW spot and the footprint-tail positions are computed at an altitude of 600±100 km above the Jovian surface, estimated by stereoscopy of PJ4 and PJ7. The positions of the two features are fitted by a Fourier expansion to determine their reference tracks. The fit is performed for each feature (MAW spot or tail) of each moon at both hemispheres separately. For each fit, the best value for the Fourier degree is estimated by computing the mean weighted sum of squared residuals (MWSSR) as function of the Fourier degree, that is:

$$MWSSR(N) = \sqrt{\frac{\sum_i W_i D_i^2}{L - (2N+1)}} \tag{1}$$

where D_i is the i-th residual (i.e: the distance between the i-th data point and the fitted curve), W_i its normalized weight, L the number of observations and N the degree of the Fourier expansion. The details of the computation of the weights in Eq.1, the uncertainty associated to the observations and the determination of the emission altitude are reported in the supporting information.

3 Results

In panel *a* and *b* of Figure 1, we report the position of the MAW spots and the footprint-tail positions respectively, alongside the results of the fitting procedure of section 2. Each point is color-coded according to its local time and two palettes were used to highlight any potential indication of local time variations. The best value for the Fourier-expansion degree N was determined to be 9 in the north and 5 in the south.

In panel *(a)* of Figure 1, in the north, only about half of each track is sampled by the JIRAM observations. JIRAM was able to observe IFP and GFP at 60°-120° and around 140° longitude respectively, while there are only a few observations for Europa around 120°. In this region, we observe deviations between the fit and JRM33+Con2020 up to ∼1000 km. Poleward deviations of about 1000 km between the GFP track and the model can also be noticed at 240°-280° longitude. In the southern hemisphere the coverage is almost complete, the largest gap being in the GFP between 0° and 40° longitude. Between 210° and 320°, the fit to the IFP, EFP and GFP are poleward of JRM33+Con2020 by up to ∼600, ∼400 and ∼200 km, respectively. Between 60° and 120° longitude, the GFP appears displaced poleward when it is observed in the dusk sector, while it is equatorward in the dawn sector. For each fit, we computed the root mean square (rms) of the residuals $R_{fit} = \sqrt{\sum_i D_i^2/L}$, which are 198, 65 and 110 km for Io, Europa and Ganymede in the north respectively, and 109, 85 and 293 km in the south.

In panel *(b)*, we report the same plots as in panel *(a)* showing the position of the footprint tails. The data coverage of the IFPT is almost complete and the only gap is around 150°-160°. This improvement is due to the long extension of the IFPT (Bonfond et al., 2017; Mura et al., 2017, 2018). All the differences between the MAW spot position and JRM33+Con2020 are also reported in the plots of panel *(b)*, as well as the transversal variability of the GFPT between 60° and 120° longitude. The rms of the residuals

R_{fit} obtained from the footprint tails are 231, 62 and 190 km for Io, Europa and Ganymede in the north respectively, and 252, 150 and 301 km in the south.

The fitted footprint tracks of panel *(a)* and *(b)* are compared in panel *(c)* and they are largely compatible within the rms of the residuals. Therefore, we suggest that both the MAW spots and the footprint tails can be used interchangeably to determine the reference ovals of the footprint tracks.

To highlight the variability of the position of the footprints, we computed the *lead angle* (Hess, Pétin, et al., 2010; Hue et al., 2023) associated with each observation. This quantity is computed by first tracing the MAW spot position along the magnetic field to the equatorial plane and then computing the angular separation with the corresponding moon at the same epoch. This quantity depends on the Alfvén travel time between the satellites and the Jovian ionosphere, so it contains information about the magnetic field and plasma mass distribution in the magnetosphere. In Figure 2, panel *(A)* and *(B)*, we report the lead angles relative to the observations of Figure 1 for the northern and southern hemisphere respectively. For each plot in both panels, the data are fitted with a periodic function $L_0 + \Delta L cos(\lambda - \phi)$, where L_0, ΔL and ϕ are free parameters and λ is the longitude of the satellites. The results of these fits are presented alongside the plots.

4 Discussion

4.1 Comparison with the JRM33+Con2020 Magnetic Field Model

We computed two predictions by expanding the spherical harmonics of JRM33 up to order 13^{th} and 18^{th}, which are the recommendations in the original work by Connerney et al. (2022), depending on the level of confidence of the magnetic field coefficients. As shown in panel *(c)* of Figure 1, the two expansions show differences in the longitude sector between 270° and 170° in the northern hemisphere. Thus, we compare the rms R_{13} and R_{18} of the distance between JIRAM data and the two JRM33+Con2020 predictions in the northern hemisphere (the two expansions lead to very similar footprint tracks in the southern hemisphere). For Io, we obtain $R_{13} = 512$ km and $R_{18} = 484$ km from the MAW spot position and $R_{13} = 424$ km and $R_{18} = 451$ km from the tail position. Indeed, in the longitude sectors 300°-330° and 100°-130°, the order 18^{th} better matches the JIRAM data, while the order 13^{th} is better between 30° and 100°. Instead, for Europa and Ganymede, R_{18} is smaller than R_{13} for both the MAW spot position and the tail positions. For Europa we obtain $R_{13} = 449$ and 549 km for the two features respectively, and $R_{18} = 320$ and 325 km, while for Ganymede $R_{13} = 609$ and 881 km, and $R_{18} = 441$ and 600 km. Therefore, we suggest expanding the JRM33 spherical harmonics up to order 18^{th} for Europa's and Ganymede's auroral emissions.

4.2 Footprint Variability: Lead Angles and Transversal Shift

The position of the MAW spots depends on the shape of the Alfvén wings, which, in turn, are determined by the magnetic field geometry and magnitude, as well as by the plasma mass density distribution in the magnetosphere. Therefore, in principle, any variation in the position of the MAW spots should be attributed to changes in either the plasma environment and/or the magnetic field. In this section, we gather the evidence of variability in the MAW spot position and we qualitatively suggest potential explanations for those observations. For this purpose, we focus on the JIRAM data acquired during different orbits but with the satellites at a similar longitude.

In the data of Figure 1 and 2, only the GFP exhibits transversal displacements. JIRAM was able to observe the GFP in both hemispheres during PJ1, PJ4, PJ7 and PJ32; among these, Ganymede orbited in the same longitude sector during both PJ1 and PJ4.

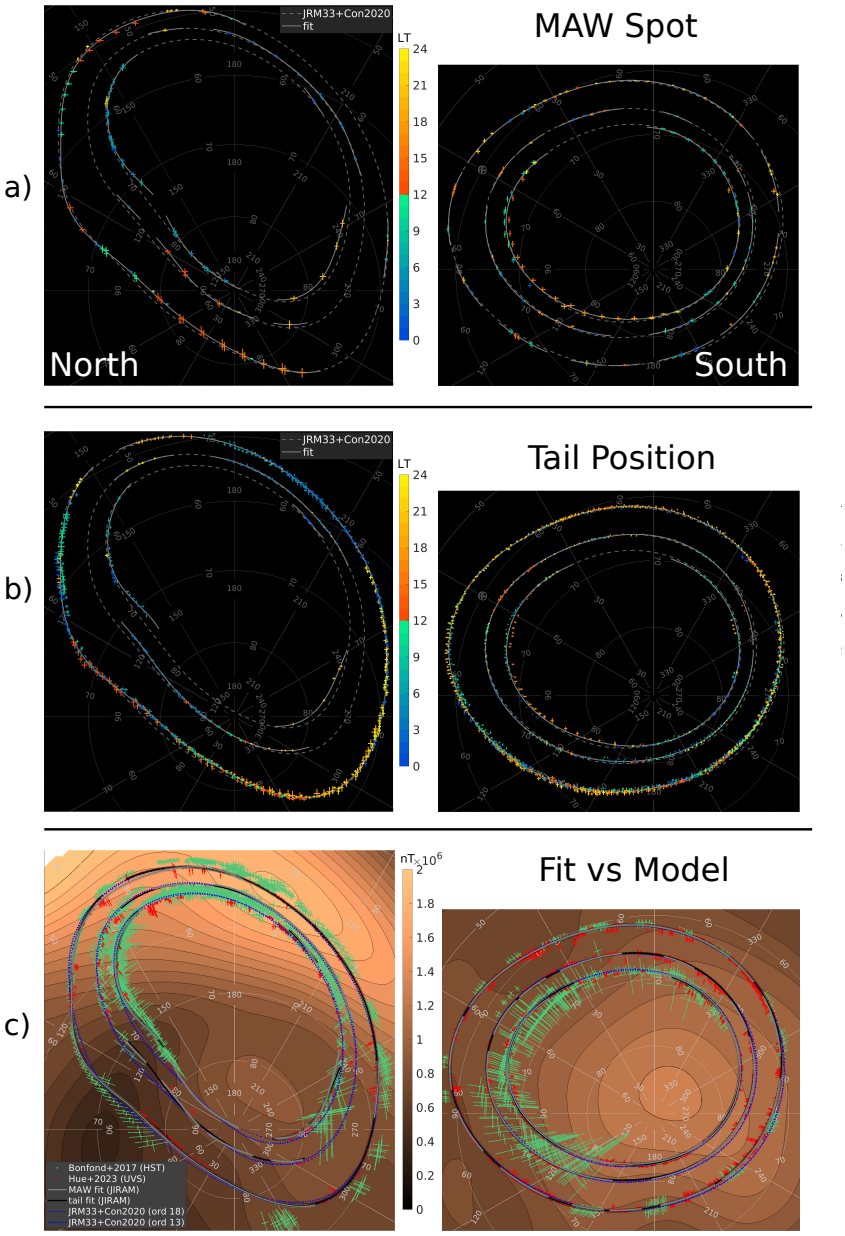

Figure 1. ***(a)*** Plot of the position of the MAW spot of Io, Europa and Ganymede in the north and south (left and right columns, respectively). The data are color-coded according to the local time of the footprint, with the cold palette for the dawn sector and the warm palette for the dusk sector. The grey continuous line is the fit to the data, the grey dashed line is the footprint track predicted by the JRM33+Con2020 magnetic field model. ***(b)*** The same as in panel *(a)*, but for the position of the footprint tails. ***(c)*** Comparison among the fits obtained from the MAW spots (grey line) and the footprint tails (black line), the JRM33+Con2020 model expanded up to order 13^{th} and 18^{th} (blue dotted and blue dashed lines, respectively) and the ultraviolet observations performed by HST (green points, from Bonfond et al. (2017)) and *Juno*-UVS (red points, from Hue et al. (2023)). The grey and black lines are surrounded by thin dotted lines of the same colors: they represent the confidence of the two fits, respectively. The background contours are the magnetic field magnitude at the surface according to JRM33+Con2020 to order 18^{th}.

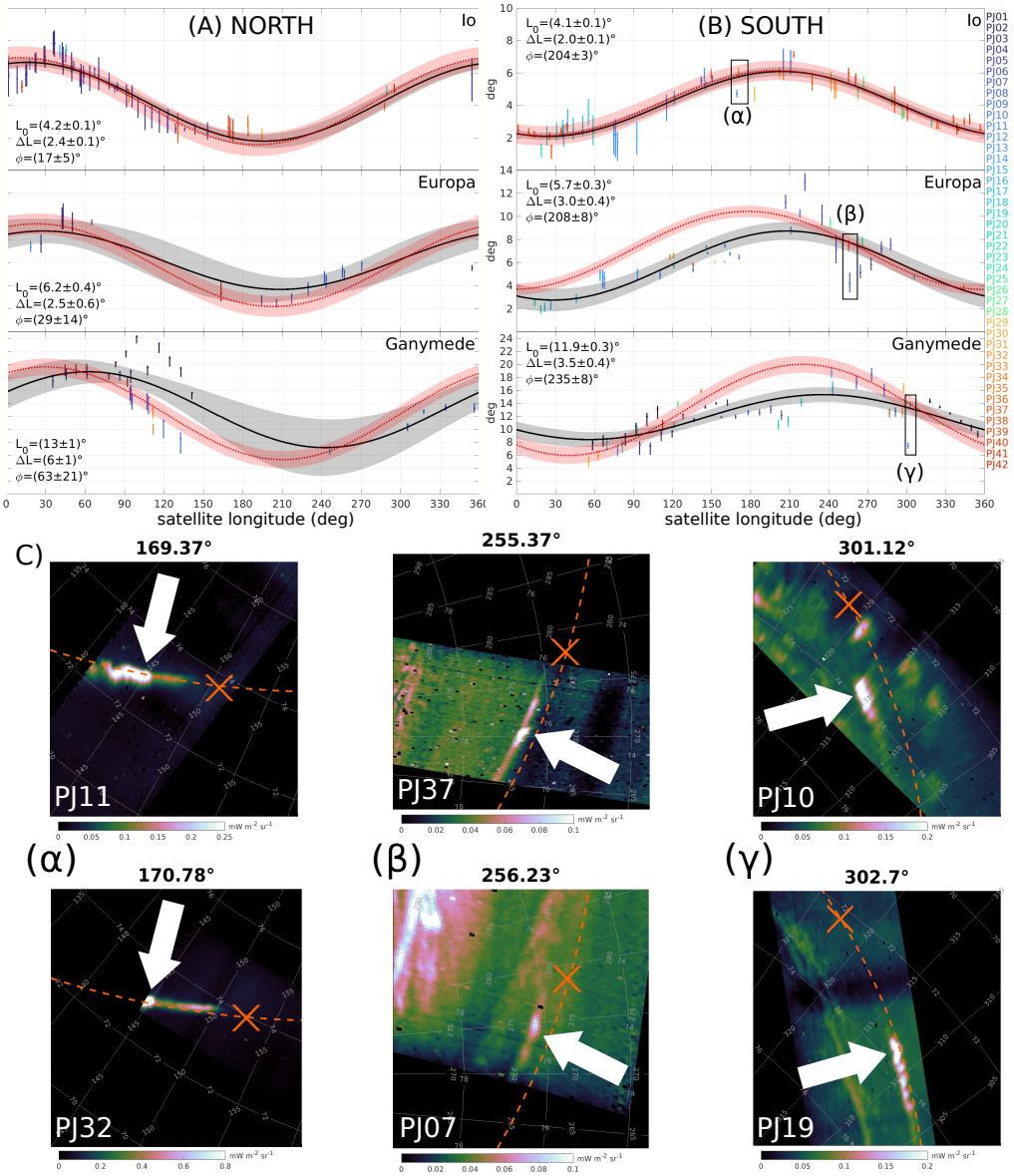

Figure 2. ***(A)***: Lead angles of the Io, Europa and Ganymede MAW spots in the northern hemisphere. The data are color-coded according the orbit number. The black line is the fit with a first-order Fourier expansion, the grey shaded area the associated 95% confidence interval. The red dotted line and the red shaded area are the fit to the lead angle derived from *Juno*-UVS observations with its uncertainty (Hue et al., 2023). In each plot, we report the parameters obtained by fitting $L_0 + \Delta Lcos(\lambda - \phi)$ to JIRAM data. ***(B)***: the same as panel *(A)*, but for the southern hemisphere. The boxes labelled α, β and γ highlight the cases of variability reported in panel *(C)*. ***(C)***: examples of variation in the MAW spot position for Io (left), Europa (center) and Ganymede (right). The orange dashed line is the satellite footprint track according to JRM33+Con2020, the cross is the magnetic footprint of each moon at the time of the acquisition of the image. The System III longitude of the satellites is reported above each image. The white arrows point to the MAW spot in each image.

The overlap of these two orbits allowed to sample the GFP track at 140° longitude and 60°-70° latitude north at two different times. No clear evidence of latitudinal displacement is observed in this region. The local time (LT) of the MAW spot observed during PJ1 and PJ4 was 4-5 hr and 7-9 hr respectively, thus both observations were in the dawn sector. In the southern hemisphere, the GFP was observed between 70° and 80° longitude during both orbits, showing a transversal displacement of 880±220 km. The LT of those observations was 11-12 hr for PJ1 (dawn sector, with the footprint equatorward displaced) and 15 hr for PJ4 (dusk sector, with the footprint poleward displaced). This suggests that the variability of the GFP position reported here might be due to a local-time asymmetry. Further evidences can be observed in the GFP and the GFPT position in the southern hemisphere at ∼165° longitude, where the emission during PJ25 (LT = 14 hr) was equatorward with respect to PJ21 (LT = 2 hr) and PJ32 (LT = 5 hr) by 370±140 km, and at 310° longitude, where the tail during PJ10 (LT = 19) was poleward with respect to PJ19 (LT = 4) and PJ33 (LT = 12 hr) by about 660±330 km. We also looked for a potential day-night correlation (not shown), but the transversal shift showed no systematic dependency with this criterion. The transversal displacement of the GFP has already been observed by HST (Grodent et al., 2008) and it have been explained by variations in the plasmadisk mass and/or radial transport (Promfu et al., 2022). Although the observations performed during PJ1 and PJ4 suggest local-time variability, we can not completely rule out a global variation of the plasmadisk. Nevertheless, this change should have occurred over less than 10 hours in order to explain the different north-south displacement observed by JIRAM. Unfortunately, JIRAM did not record the GFP crossing from the dawn to the dusk sector (or vice-versa), which might have represented stronger evidence of its local-time variability.

The lead angle shown in Figure 2 can help to detect evidence of longitudinal variability between different orbits. In the northern hemisphere (panel *(A)*), we report a single case for Io at ∼290° between PJ20 and PJ34, and one for Ganymede between 90° and 135°, where the lead angle of PJ1 was larger than the one of PJ4, PJ9, PJ32 and PJ37. In the southern hemisphere (panel *(B)*), we identified several cases that show different lead angle at the same satellite longitude: for Io there is PJ11-PJ32 at 170° longitude; for Europa PJ18-PJ32 at 120°, PJ8-PJ40 at 135°, PJ14-PJ29 at 160°, PJ7-PJ37 at 255° and PJ7-PJ26 at 265°; for Ganymede PJ1-PJ4 between 90° and 120°, PJ4-PJ7 at 160° and PJ30-PJ33 and PJ10-PJ19, both around 300°. For each satellite, we select one example pair of observations, labelled α, β and γ in panel *(B)*, and the corresponding images are reported in panel *(C)*. Case α shows the IFP during PJ11 and PJ32, with lead angles 4.7±0.2° and 6.0±0.3°, respectively. Additionally, the distance between the MAW spot and the tip of the leading spot to the right of the MAW spot, which is associated to the electron beam accelerated above the ionosphere at the opposite hemisphere (Bonfond et al., 2008; Hess, Delamere, et al., 2010), is about 1000 km and 1700 km respectively. This pair of observations was analyzed in Moirano et al. (2023), where the difference was attributed either to changes in the state of the Io Plasma Torus (Bagenal & Dols, 2020) between the two orbits or to the local-time asymmetry of the plasma torus. Case β shows the longitudinal displacement of the EFP by comparing PJ7 and PJ37, when the lead angle was 4.3±0.8° and 7.5±0.5° respectively, while Europa was at the same longitude within less than 1°. Similarly, in case γ, the GFP exhibits both transversal and longitudinal displacement by comparing PJ10 and PJ19 (lead angle 7.5±0.5° and 13.8±0.5°, respectively). Although the transversal displacement in case γ can be ascribed to a local time asymmetry as discussed in the previous paragraph, we found no clear dependency of the lead angle on the local time.

The longitudinal and the transversal displacements of the footprints can be explained by two different processes. The longitudinal displacement at a given satellite longitude can be caused by a change in the Alfvén travel time - which corresponds to a variation in the plasma environment - or to a change in the radial current of the plasmadisk - which causes an azimuthal stretch of the magnetic field lines. On the other hand, a transver-

sal displacement can be explained by the satellites connecting to different magnetic shells, which can be due to variations in the azimuthal component of the magnetodisk current that radially stretches the magnetic field. We estimated the longitudinal and transversal displacement by changing the radial current of the Con2020 model $\mu_0 I_R/2\pi$ between 7.7 and 35.2 MA, and the azimuthal current $\mu_0 I_{MD}/2$ between 124.2 and 156.1 nT, according to the *Juno* magnetometer data (Connerney et al., 2020). The longitudinal shift caused by the radial current variations is approximately 70, 200 and 450 km for Io, Europa and Ganymede respectively, while the transversal shift is about 100, 250 and 650 km. For Io and Europa, these values are similar to or smaller than the footprint size; hence it appears unlikely that the variability observed at those moons is caused by changes in the plasmadisk currents. Furthermore, both the IFP and EFP exhibited lead angle variations, but no transversal variation, which suggests variations in the plasma environment around the two satellites. On the other hand, the GFP displacement in Figure 1 may be compatible with magnetodisk variations such as the ones detected by the *Juno* magnetometer. Thus, we suggest that the variations in the GFP position can be caused either by local time asymmetry and temporal variations of the magnetodisk currents or changes in the plasmadisk mass content.

4.3 Comparison with *Juno*-UVS and HST Observations

In panel *(c)* of Figure 1, we compare the fit obtained from the MAW spot and tail positions against the ultraviolet observations performed by HST (Bonfond et al., 2017) and *Juno*-UVS (Hue et al., 2023). For the IFP in the northern hemisphere, the HST observations are systematically equatorward with respect to both the JIRAM-based fits and UVS data. The HST, JIRAM and UVS osbervations of the GFP at ∼140° longitude, 65°-80° latitude are consistent, while they are only marginally in agreement with JRM33+Con2020. In the south, the HST observations usually lie equatorward with respect to the *Juno* measurements roughly between 30° and 120° longitude, while at the other longitudes the data from the two spacecrafts agree within the HST uncertainty. The HST data of the GFP between 40° and 60° longitude seems to suggest a transversal shift of the GFP of about 2400 km between September 2009 (poleward) and December 2000, January 2001 and May 2007 (equatorward). We inspected the local-time distribution of these four set, of observations, but we found no clear evidence of local-time dependency as in the JIRAM data. Lastly, the lack of observations in the northern hemisphere during September 2009 prevents a north-south comparison of this shift.

The referencing of the HST images onto the Jovian surface is radically different from the one used for *Juno*. For HST, the inferred position of the footprints relies on the localization of the planetary center, which in turn is determined by fitting the planetary limb in the HST images themselves (Bonfond et al., 2009). On the other hand, *Juno*-based observations are localized using the spacecraft ephemeris and the instrument pointing, which are provided by the Navigation and Ancillary Information Facility (NAIF, C. H. Acton (1996); C. Acton et al. (2018)). Therefore, the different referencing procedures for HST and *Juno* might be the root cause of the discrepancy among the observations performed by the two spacecrafts. Now, thanks to the fits in Figure 1, it becomes possible to automatically compute the location of Jupiter's center relative to the IFP MAW spot for any HST image in which the Io footprint is visible and use this spot to improve significantly the referencing accuracy. This new method assumes that the location of the MAW spot is stable through time at resolution of HST and it can not be used to further study subtle variations of the MAW spot location as a function of the torus state. Nevertheless, both the data shown in Figure 1 and the Io lead angle in Figure 2 suggest that the IFP position varies only occasionally, thus we believe that its MAW spot is a reliable reference.

The *Juno*-UVS data in Figure 1 are very consistent with the JIRAM fits. The UVS observation of the IFP between 60° and 120° longitude performed during PJ8, PJ12, PJ15

and PJ18 matches very well the fits in the same region, which was observed by JIRAM during PJ4, PJ7, PJ15 and PJ18. The UV and IR measurements also agree between 250° and 290° longitude of the GFP, where they both show a poleward displacement with respect to JRM33+Con2020. UVS data shows the transversal displacement in the GFP at ∼75°-90° longitude, where the GFP was displaced poleward during PJ7 (LT = 18 hr) with respect to PJ27 (LT = 8). Unfortunately, no measurements are reported in the northern hemisphere during those PJs for comparison. In Figure 2, the lead angle derived from JIRAM data is compared with the one from UVS data. For Io, the sinusoidal fit to the lead angle appears almost symmetric between the two hemispheres, apart from a phase difference of 187±8°, and it matches the result obtained by UVS. The lead angle phases are consistent with the tilt of the centrifugal equator towards ∼200° longitude (Moirano, Gomez Casajus, et al., 2021; Phipps et al., 2020) and the consequent wiggling up and down of Io within the Io Plasma Torus. The Europa lead angle derived in the northern hemisphere is also compatible with the southern one, the phase difference between the two being ∼179±22°. The phase of the fit to the lead angle is also compatible with the position of the centrifugal equator, showing a maximum at 29±14° in the north and 208±8° in the south. The UVS results shows a larger lead angle overall, and the southern hemisphere the phase difference between JIRAM and UVS is about 20°. At Ganymede, the amplitude of the lead angle in the northern hemisphere is larger than the amplitude in the south ($\Delta L = 6\pm1°$ and 3.5±0.4°, respectively), and the two fits are out of phase by 172±29°. Unlike the Io and Europa lead angles, the Ganymede lead angle peaks at 63±21° in the north and 235±8° in the south, while UVS data reported ∼30° and ∼220°, respectively. The differences between the JIRAM and UVS lead angles at Europa and Ganymede might be due to the different coverages between the two instrument, combined with the intrinsic variability of these footprints. Despite these differences, both datasets are overall consistent with the geometry of the Jovian magnetosphere and its plasma distribution.

5 Conclusions

We reported the *Juno*-JIRAM infrared observation of the Io, Europa and Ganymede auroral footprints observed over 42 spacecraft orbits, between August 2016 and May 2022. The main goal is to provide the reference tracks for the three footprints. Further results of this work can be summarized as follow:

- The *Juno*-based magnetic field model JRM33+Con2020 (Connerney et al., 2020, 2022; Wilson et al., 2023) precisely predict the footprint tracks, although variations up to ∼1000 km are reported between 60° and 140° longitude in the northern hemisphere, as well as deviations up to ∼600km between 210° and 320° longitude in the south.
- All three footprints exhibit evidence of longitudinal variability, which can be inferred by computing their lead angles. However, only the GFP shows clear evidence of transversal variations, which appear to be local-time dependent.
- The transversal shift of the GFP might be explained by variations in the external magnetic field due to the plasmadisk current, which radially stretches the magnetic field outwards.
- The positions of the MAW spots from JIRAM agree very well with the *Juno*-UVS observations, while the positions derived from HST campaigns are occasionally systematically displaced (such as the IFP north).
- The Io lead angle derived here is in good agreement with the lead angle from *Juno*-UVS data, as well as the Europa lead angle in the northern hemisphere. Instead, amplitude and phase deviations between the two datasets are observed for the EFP in the south and for the GFP in both hemispheres.

Open Research Section

JIRAM data and materials used in this study are publicly available on the Planetary Data System (https://pds-atmospheres.nmsu.edu/data_and_services/atmospheres_data/JUNO/jiram.html). The repository for the data products used in this study is :https://doi.org/10.5281/zenodo.7924394 (Moirano, 2023).

Acknowledgments

The authors thank Agenzia Spaziale Italiana (ASI) for supporting the JIRAM contribution to the Juno mission (including this work) under the ASI contract 2016-23-H.0. This publication benefits from the support of the French Community of Belgium in the context of the FRIA Doctoral Grant awarded to L.H.

References

Acton, C., Bachman, N., Semenov, B., & Wright, E. (2018, January). A look towards the future in the handling of space science mission geometry. *Planetary and Space Science*, *150*, 9–12. doi: 10.1016/j.pss.2017.02.013

Acton, C. H. (1996, January). Ancillary data services of NASA's Navigation and Ancillary Information Facility. *Planetary and Space Science*, *44*(1), 65–70. doi: 10.1016/0032-0633(95)00107-7

Acuña, M. H., Neubauer, F. M., & Ness, N. F. (1981, September). Standing Alfvén wave current system at Io: Voyager 1 observations. *J. Geophys. Res.*, *86*(A10), 8513–8521. doi: 10.1029/JA086iA10p08513

Adriani, A., Filacchione, G., Di Iorio, T., Turrini, D., Noschese, R., Cicchetti, A., ... Olivieri, A. (2017, November). JIRAM, the Jovian Infrared Auroral Mapper. *Space Sci Rev*, *213*(1-4), 393–446. doi: 10.1007/s11214-014-0094-y

Bagenal, F., Adriani, A., Allegrini, F., Bolton, S. J., Bonfond, B., Bunce, E. J., ... Zarka, P. (2017, November). Magnetospheric Science Objectives of the Juno Mission. *Space Sci Rev*, *213*(1-4), 219–287. doi: 10.1007/s11214-014-0036-8

Bagenal, F., & Dols, V. (2020, May). The Space Environment of Io and Europa. *J. Geophys. Res. Space Physics*, *125*(5). doi: 10.1029/2019JA027485

Belcher, J. W., Goertz, C. K., Sullivan, J. D., & Acuña, M. H. (1981). Plasma observations of the Alfvén wave generated by Io. *Journal of Geophysical Research: Space Physics*, *86*(A10), 8508–8512. doi: 10.1029/JA086iA10p08508

Bhattacharyya, D., Clarke, J. T., Montgomery, J., Bonfond, B., Gérard, J., & Grodent, D. (2018, January). Evidence for Auroral Emissions From Callisto's Footprint in HST UV Images. *J. Geophys. Res. Space Physics*, *123*(1), 364–373. doi: 10.1002/2017JA024791

Bonfond, B., Grodent, D., Gérard, J.-C., Radioti, A., Dols, V., Delamere, P. A., & Clarke, J. T. (2009, July). The Io UV footprint: Location, inter-spot distances and tail vertical extent. *J. Geophys. Res.*, *114*(A7), n/a–n/a. doi: 10.1029/2009JA014312

Bonfond, B., Grodent, D., Gérard, J.-C., Radioti, A., Saur, J., & Jacobsen, S. (2008, March). UV Io footprint leading spot: A key feature for understanding the UV Io footprint multiplicity? *Geophys. Res. Lett.*, *35*(5), L05107. doi: 10.1029/2007GL032418

Bonfond, B., Saur, J., Grodent, D., Badman, S. V., Bisikalo, D., Shematovich, V., ... Radioti, A. (2017, August). The tails of the satellite auroral footprints at Jupiter. *J. Geophys. Res. Space Physics*, *122*(8), 7985–7996. doi: 10.1002/2017JA024370

Clarke, J. T., Ajello, J., Ballester, G., Ben Jaffel, L., Connerney, J., Gérard, J.-C., ... Waite, J. H. (2002, February). Ultraviolet emissions from the magnetic footprints of Io, Ganymede and Europa on Jupiter. *Nature*, *415*(6875), 997–1000. doi: 10.1038/415997a

Clarke, J. T., Ballester, G. E., Trauger, J., Evans, R., Connerney, J. E. P., Stapelfeldt, K., ... Westphal, J. A. (1996, October). Far-Ultraviolet Imaging of Jupiter's Aurora and the Io "Footprint". *Science*, *274*(5286), 404–409. doi: 10.1126/science.274.5286.404

Connerney, J. E. P., Adriani, A., Allegrini, F., Bagenal, F., Bolton, S. J., Bonfond, B., ... Waite, J. (2017, May). Jupiter's magnetosphere and aurorae observed by the Juno spacecraft during its first polar orbits. *Science*, *356*(6340), 826–832. doi: 10.1126/science.aam5928

Connerney, J. E. P., Baron, R., Satoh, T., & Owen, T. (1993, November). Images of Excited H3+ at the Foot of the Io Flux Tube in Jupiter's Atmosphere. *Science*, *262*(5136), 1035–1038. doi: 10.1126/science.262.5136.1035

Connerney, J. E. P., Timmins, S., Herceg, M., & Joergensen, J. L. (2020). A Jovian Magnetodisc Model for the Juno Era. *Journal of Geophysical Research: Space Physics*, *125*(10), e2020JA028138. doi: 10.1029/2020JA028138

Connerney, J. E. P., Timmins, S., Oliversen, R. J., Espley, J. R., Joergensen, J. L., Kotsiaros, S., ... Levin, S. M. (2022). A New Model of Jupiter's Magnetic Field at the Completion of Juno's Prime Mission. *Journal of Geophysical Research: Planets*, *127*(2), e2021JE007055. doi: 10.1029/2021JE007055

Damiano, P. A., Delamere, P. A., Stauffer, B., Ng, C.-S., & Johnson, J. R. (2019). Kinetic Simulations of Electron Acceleration by Dispersive Scale Alfvén Waves in Jupiter's Magnetosphere. *Geophysical Research Letters*, *46*(6), 3043–3051. doi: 10.1029/2018GL081219

Drell, S. D., Foley, H. M., & Ruderman, M. A. (1965, February). Drag and Propulsion of Large Satellites in the Ionosphere; An Alfv\'en Propulsion Engine in Space. *Physical Review Letters*, *14*(6), 171–175. doi: 10.1103/PhysRevLett.14.171

Drossart, P., Maillard, J., Caldwell, J., Kim, S., Watson, J., Majewski, W., ... Wagener, R. (1989, August). Detection of H3+ on Jupiter. *Nature*, *340*. doi: 10.1038/340539a0

Gladstone, G. R., Stern, S. A., Slater, D. C., Versteeg, M., Davis, M. W., Retherford, K. D., ... Nichols, J. D. (2007, October). Jupiter's Nightside Airglow and Aurora. *Science*, *318*(5848), 229–231. doi: 10.1126/science.1147613

Gladstone, G. R., Waite, J. H., Grodent, D., Lewis, W. S., Crary, F. J., Elsner, R. F., ... Cravens, T. E. (2002, February). A pulsating auroral X-ray hot spot on Jupiter. *Nature*, *415*(6875), 1000–1003. doi: 10.1038/4151000a

Grodent, D. (2015, April). A Brief Review of Ultraviolet Auroral Emissions on Giant Planets. *Space Sci Rev*, *187*(1-4), 23–50. doi: 10.1007/s11214-014-0052-8

Grodent, D., Gérard, J.-C., Gustin, J., Mauk, B. H., Connerney, J. E. P., & Clarke, J. T. (2006). Europa's FUV auroral tail on Jupiter. *Geophysical Research Letters*, *33*(6). doi: https://doi.org/10.1029/2005GL025487

Grodent, D., Gérard, J.-C., Radioti, A., Bonfond, B., & Saglam, A. (2008). Jupiter's changing auroral location. *Journal of Geophysical Research: Space Physics*, *113*(A1). doi: 10.1029/2007JA012601

Hess, S. L. G., Delamere, P., Dols, V., Bonfond, B., & Swift, D. (2010, June). Power transmission and particle acceleration along the Io flux tube. *J. Geophys. Res.*, *115*(A6), n/a–n/a. doi: 10.1029/2009JA014928

Hess, S. L. G., Pétin, A., Zarka, P., Bonfond, B., & Cecconi, B. (2010, August). Lead angles and emitting electron energies of Io-controlled decameter radio arcs. *Planetary and Space Science*, *58*(10), 1188–1198. doi: 10.1016/j.pss.2010.04.011

Hill, T. (1979). Inertial limit on corotation. *J. Geophys. Res.*, *84*(A11), 6554. doi: 10.1029/JA084iA11p06554

Hinton, P. C., Bagenal, F., & Bonfond, B. (2019). Alfvén Wave Propagation in the Io Plasma Torus. *Geophysical Research Letters*, *46*(3), 1242–1249. doi: 10.1029/2018GL081472

Hue, V., Gladstone, G. R., Louis, C. K., Greathouse, T. K., Bonfond, B., Szalay, J. R., ... Connerney, J. (2023). The Io, Europa and Ganymede auroral footprints at Jupiter in the ultraviolet: Positions and equatorial lead angles. *Journal of Geophysical Research: Space Physics*, *n/a*(n/a), e2023JA031363. doi: 10.1029/2023JA031363

Jones, S. T., & Su, Y.-J. (2008). Role of dispersive Alfvén waves in generating parallel electric fields along the Io-Jupiter fluxtube. *Journal of Geophysical Research: Space Physics*, *113*(A12). doi: https://doi.org/10.1029/2008JA013512

Kivelson, M. G., Bagenal, F., Kurth, W. S., Neubauer, F. M., Paranicas, C., & Saur, J. (2004). Magnetospheric Interactions with Satellites. In *Jupiter: The Planet, Satellites and Magnetosphere* (F. Bagenal ed., Vol. 21, p. 513). Cambridge UK: Cambridge Univ. Press.

Kurth, W. S., Imai, M., Hospodarsky, G. B., Gurnett, D. A., Louarn, P., Valek, P., ... Zarka, P. (2017). A new view of Jupiter's auroral radio spectrum. *Geophysical Research Letters*, *44*(14), 7114–7121. doi: 10.1002/2017GL072889

Miller, S., Tennyson, J., Geballe, T. R., & Stallard, T. (2020, August). Thirty years of H 3 + astronomy. *Rev. Mod. Phys.*, *92*(3), 035003. doi: 10.1103/RevModPhys.92.035003

Moirano, A. (2023, May). *Data for the research article: "The Infrared Footprint Tracks of Io, Europa and Ganymede at Jupiter Observed by Juno-JIRAM".* Zenodo. doi: 10.5281/zenodo.7924394

Moirano, A., Gomez Casajus, L., Zannoni, M., Durante, D., & Tortora, P. (2021). Morphology of the Io Plasma Torus From Juno Radio Occultations. *Journal of Geophysical Research: Space Physics*, *126*(10), e2021JA029190. doi: 10.1029/2021JA029190

Moirano, A., Mura, A., Adriani, A., Dols, V., Bonfond, B., Waite, J. H., ... Bolton, S. J. (2021). Morphology of the Auroral Tail of Io, Europa, and Ganymede From JIRAM L-Band Imager. *Journal of Geophysical Research: Space Physics*, *126*(9), e2021JA029450. doi: 10.1029/2021JA029450

Moirano, A., Mura, A., Bonfond, B., Connerney, J., Dols, V., Grodent, D., ... Zambon, F. (2023). Manuscript #2023JA031288 Variability of the Auroral Footprint of Io Detected by Juno-JIRAM and Modelling of the Io Plasma Torus. *Journal of Geophysical Research: Space Physics*.

Mura, A., Adriani, A., Altieri, F., Connerney, J. E. P., Bolton, S. J., Moriconi, M. L., ... Olivieri, A. (2017, June). Infrared observations of Jovian aurora from Juno's first orbits: Main oval and satellite footprints: Jovian Aurora IR Observations From Juno. *Geophys. Res. Lett.*, *44*(11), 5308–5316. doi: 10.1002/2017GL072954

Mura, A., Adriani, A., Connerney, J. E. P., Bolton, S., Altieri, F., Bagenal, F., ... Turrini, D. (2018, August). Juno observations of spot structures and a split tail in Io-induced aurorae on Jupiter. *Science*, *361*(6404), 774–777. doi: 10.1126/science.aat1450

Natan, A. (2021). *Fast 2D Peak Finder.*

Neubauer, F. (1980, March). Nonlinear standing Alfvén wave current system at Io: Theory. *J. Geophys. Res.*, *85*(A3), 1171–1178. doi: 10.1029/JA085iA03p01171

Phipps, P. H., Withers, P., Vogt, M. F., Buccino, D. R., Yang, Y., Parisi, M., ... Bolton, S. (2020, August). Where Is the Io Plasma Torus? A Comparison of Observations by Juno Radio Occultations to Predictions From Jovian Magnetic Field Models. *J. Geophys. Res. Space Physics*, *125*(8). doi: 10.1029/2019JA027633

Prangé, R., Rego, D., Southwood, D., Zarka, P., Miller, S., & Ip, W. (1996, January). Rapid energy dissipation and variability of the lo–Jupiter electrodynamic circuit. *Nature*, *379*(6563), 323–325. doi: 10.1038/379323a0

Promfu, T., Nichols, J. D., Wannawichian, S., Clarke, J. T., Vogt, M. F., & Bon-

fond, B. (2022). Ganymede's Auroral Footprint Latitude: Comparison With Magnetodisc Model. *Journal of Geophysical Research: Space Physics*, *127*(12), e2022JA030712. doi: 10.1029/2022JA030712

Saur, J. (2004). A model of Io's local electric field for a combined Alfvénic and unipolar inductor far-field coupling. *Journal of Geophysical Research: Space Physics*, *109*(A1). doi: 10.1029/2002JA009354

Sulaiman, A. H., Hospodarsky, G. B., Elliott, S. S., Kurth, W. S., Gurnett, D. A., Imai, M., ... Bolton, S. J. (2020, August). Wave-particle interactions associated with Io's auroral footprint: Evidence of Alfvén, ion cyclotron, and whistler modes. *Geophys. Res. Lett.*. doi: 10.1029/2020GL088432

Trafton, L., Carr, J., Lester, D., & Harvey, P. (1989). Jupiter's Aurora: Detection of Quadrupole h2 Emission. *NASA Special Publication*, *494*.

Wilson, R. J., Vogt, M. F., Provan, G., Kamran, A., James, M. K., Brennan, M., & Cowley, S. W. H. (2023, February). Internal and External Jovian Magnetic Fields: Community Code to Serve the Magnetospheres of the Outer Planets Community. *Space Science Reviews*, *219*(1), 15. doi: 10.1007/s11214-023-00961-3

Supporting Information for "The Infrared Footprint Tracks of Io, Europa and Ganymede at Jupiter Observed by *Juno*-JIRAM"

A. Moirano[1,2], A. Mura[1], V. Hue[3,4], B. Bonfond[5,6], L. A. Head[5,6], J.E.P. Connerney[7], A. Adriani[1], F. Altieri[1], C. Castagnoli[1,8,9], A. Cicchetti[1], B. M. Dinelli[8], D. Grassi[1], A. Migliorini[1], M. L. Moriconi[1], R. Noschese[1], G. Piccioni[1], C. Plainaki[10], P. Scarica[1], G. Sindoni[10], R. Sordini[1], F. Tosi[1], D. Turrini[1], F. Zambon[1]

[1]Institute for Space Astrophysics and Planetology, National Institute for Astrophysics (INAF—IAPS), Rome, Italy

[2]Sapienza University of Rome, Rome, Italy

[3]Aix-Marseille Université, CNRS, CNES, Institut Origines, LAM, Marseille, France

[4]southwest Research Institute, San Antonio, Texas, USA

[5]Laboratory for Planetary and Atmospheric Physics, Space Science, Technologies and Astrophysical Research Institute, University of Liège, Liège, Belgium

[6]Space sciences, Technologies and Astrophysics Research Institute, Université de Liège, Belgium

[7]Space Research Corporation, Annapolis, MD, USA

[8]Institute of Atmospheric Sciences and Climate, National Research Council (CNR - ISAC), Bologna, Italy

[9]University of Rome Tor Vergata, Rome, Italy

[10]Italian Space Agency (ASI), Rome, Italy

Contents of this file

1. Text S1

Additional Supporting Information (Files uploaded separately)

1. Captions for Table S1 to S24

Introduction

This supporting information Text S1 explains how the infrared altitude of the footprints is estimated and how the uncertainty of its position are evaluated.

The Data Sets S1-S6 contains the fit to the Main Alfvén Wing spot position of Io, Europa and Ganymede as they are shown in Figure 1 of the main text. The coordinates of the Ganymede footprint as function of the satellite longitude (Table S5 and S6) exhibit oscillations that are due to the intrinsic variability of the footprint position. The Europa footprint (Table S3 and S4) also exhibits a similar behaviour, although to a much lesser extent. We did not filter this oscillations out to not introduce an additional layer of data processing, which is left to the reader's needs. The Data Sets S7-S12 contain the fit to the footprint tail position of the three moons.

The Data Sets S13-S18 contain the position of the Main Alfvén Wing spot of Io, Europa and Ganymede derived from the JIRAM images, and the Data Sets S19-S24 the respective footprint-tail position.

Text S1.

To properly determine the coordinates of the peak of the emission, we need to estimate its expected altitude. JIRAM observed the IFP during PJ 4 and 7 between 90° and 120° in the northern hemisphere with two different emission angles of ∼75° and ∼35° respectively (this is the angle between the normal to the planetary surface and the instrument line of sight). By stereoscopy, it is possible to determine the altitude of the emission, which is estimated to peak at 600±100 km. According to chemistry models (Tao et al., 2011), the IR emission peaks between 500 and 1000 km for precipitating electrons with energy between 0.1 and 100 keV. The *Juno*-JADE-E particle detector measured the energy of the precipitating electrons associated with Io (Sulaiman et al., 2020; Szalay et al., 2020b), Europa (Allegrini et al., 2020) and Ganymede (Szalay et al., 2020a). The energy distribution associated with each moon shows remarkable similarity with each other, with a broadband spectrum and the bulk of electrons at energy < 1 keV. Because of this and the weak dependency of the peak altitude with the precipitating electron energy, we conclude that the IR emission of both the MAW spots and the footprint tails of all three satellite is expected to occur at an altitude of 600±100 km. The associated Δ_h in Eq.2 of the main text is then computed by projecting the ±100 km uncertainty along the line of sight of JIRAM.

The uncertainty associated with the JIRAM observations takes into account three contributions, namely: 1) the uncertainty on the altitude of the emission, 2) the physical size of the MAW spot and 3) the resolution of the image. The uncertainty Δ_k (k being an xyz

coordinate) on the position of the MAW spots is then computed as

$$\Delta_k = \sqrt{\Delta^2_{h(k)} + \Delta^2_{size(k)} + \Delta^2_{res(k)}} \tag{1}$$

where the three term on the rhs are the above-mentioned source of uncertainty.

The uncertainty $\Delta_{h(k)}$ is computed by using the instrument pointing provided by the Navigation and Ancillary Information Facility (NAIF, C. H. Acton (1996); C. Acton, Bachman, Semenov, and Wright (2018)) and by referencing the images at surfaces at the different altitudes of 600±100 km.

The longitudinal and transversal size of the MAW spots (Δ_{size}) is estimated from images captured at an emission angles <15°, while we selected images at emission angles >70° for the vertical extension. Unluckily, no images of the GFP at high emission angle are available. Nevertheless, the energy distribution of the precipitating electrons associated with the GFP is similar to the distribution of the EFP and IFP, thus we can assume that the vertical extension of the GFP is also similar to the other two. The longitudinal-transversal-vertical size of the IFP is (438±156)-(154±16)-(382±76) km, while for the EFP we obtain (538±206)-(202±24)-(502±360). The GFP longitudinal and transversal sizes are (958±120) and (200±42) respectively, and we assumed that its vertical extension is 400 km. The higher longitudinal size of the GFP is due to the presence of two lobes in the MAW spot, which are potentially caused by the geometry of the intrinsic magnetic field of Ganymede.

The weight in Eq. 1 of the main text are computed as

$$w_i = \frac{1}{\Delta^2_x + \Delta^2_y + \Delta^2_z} \tag{2}$$

and then they are normalized as

$$W_i = \frac{w_i}{\sum_i w_i} \tag{3}$$

Table S1.

System III spherical coordinates of the Main Alfvén Wing spot of Io in the northern hemisphere, corresponding to the continuous grey line in Figure 1 in the main text. The first column is the satellite longitude in degrees, the second the radial distance in km from Jupiter's center, the third and fourth the footprint longitude and planetocentric latitude in degrees respectively.

Table S2.

System III spherical coordinates of the Main Alfvén Wing spot of Io in the southern hemisphere, corresponding to the continuous grey line in Figure 1 in the main text. The first column is the satellite longitude in degrees, the second the radial distance in km from Jupiter's center, the third and fourth the footprint longitude and planetocentric latitude in degrees respectively.

Table S3.

System III spherical coordinates of the Main Alfvén Wing spot of Europa in the northern hemisphere, corresponding to the continuous grey line in Figure 1 in the main text. The first column is the satellite longitude in degrees, the second the radial distance in km from Jupiter's center, the third and fourth the footprint longitude and planetocentric latitude in degrees respectively.

Table S4.

System III spherical coordinates of the Main Alfvén Wing spot of Europa in the southern

hemisphere, corresponding to the continuous grey line in Figure 1 in the main text. The first column is the satellite longitude in degrees, the second the radial distance in km from Jupiter's center, the third and fourth the footprint longitude and planetocentric latitude in degrees respectively.

Table S5.

System III spherical coordinates of the Main Alfvén Wing spot of Ganymede in the northern hemisphere, corresponding to the continuous grey line in Figure 1 in the main text. The first column is the satellite longitude in degrees, the second the radial distance in km from Jupiter's center, the third and fourth the footprint longitude and planetocentric latitude in degrees respectively.

Table S6.

System III spherical coordinates of the Main Alfvén Wing spot of Ganymede in the southern hemisphere, corresponding to the continuous grey line in Figure 1 in the main text. The first column is the satellite longitude in degrees, the second the radial distance in km from Jupiter's center, the third and fourth the footprint longitude and planetocentric latitude in degrees respectively.

Table S7.

System III spherical coordinates of the Io footprint tail in the northern hemisphere, corresponding to the continuous grey line in panel *(b)* and the continuous black line in panel *(c)* of Figure 1 in the main text. The first column the radial distance in km from Jupiter's center, the second and third the footprint tail longitude and planetocentric latitude in degrees respectively.

Table S8.

System III spherical coordinates of the Io footprint tail in the southern hemisphere, corresponding to the continuous grey line in panel *(b)* and the continuous black line in panel *(c)* of Figure 1 in the main text. The first column the radial distance in km from Jupiter's center, the second and third the footprint tail longitude and planetocentric latitude in degrees respectively.

Table S9.

System III spherical coordinates of the Europa footprint tail in the northern hemisphere, corresponding to the continuous grey line in panel *(b)* and the continuous black line in panel *(c)* of Figure 1 in the main text. The first column the radial distance in km from Jupiter's center, the second and third the footprint tail longitude and planetocentric latitude in degrees respectively.

Table S10.

System III spherical coordinates of the Europa footprint tail in the southern hemisphere, corresponding to the continuous grey line in panel *(b)* and the continuous black line in panel *(c)* of Figure 1 in the main text. The first column the radial distance in km from Jupiter's center, the second and third the footprint tail longitude and planetocentric latitude in degrees respectively.

Table S11.

System III spherical coordinates of the Ganymede footprint tail in the northern hemisphere, corresponding to the continuous grey line in panel *(b)* and the continuous black line in panel *(c)* of Figure 1 in the main text. The first column the radial distance in km from Jupiter's center, the second and third the footprint tail longitude and planetocentric latitude in degrees respectively.

Table S12.

System III spherical coordinates of the Ganymede footprint tail in the southern hemisphere, corresponding to the continuous grey line in panel *(b)* and the continuous black line in panel *(c)* of Figure 1 in the main text. The first column the radial distance in km from Jupiter's center, the second and third the footprint tail longitude and planetocentric latitude in degrees respectively.

Table S13.

Cartesian coordinates in km of the Io footprint in the northern hemisphere, corresponding to the data points in Figure 1 of the main text. The first column contains the perijove (PJ) number, the second the hemisphere observed. The third, fourth and fifth columns contain the date of the observation, while the sixth and seventh columns are the starting and ending time of the observation, respectively (they coincide for the Main Alfvén Wing spot observations). The X, Y and Z System-III coordinates of the spot are reported in column 8, 9 and 10. The last six columns contain the upper (up) and lower (dw) error on the spot position.

Table S14.

Cartesian coordinates in km of the Io footprint in the southern hemisphere, corresponding to the data points in Figure 1 of the main text. The first column contains the perijove (PJ) number, the second the hemisphere observed. The third, fourth and fifth columns contain the date of the observation, while the sixth and seventh columns are the starting and ending time of the observation, respectively (they coincide for the Main Alfvén Wing spot observations). The X, Y and Z System-III coordinates of the spot are reported in column 8, 9 and 10. The last six columns contain the upper (up) and lower (dw) error on

the spot position.

Table S15.

Cartesian coordinates in km of the Europa footprint in the northern hemisphere, corresponding to the data points in Figure 1 of the main text. The first column contains the perijove (PJ) number, the second the hemisphere observed. The third, fourth and fifth columns contain the date of the observation, while the sixth and seventh columns are the starting and ending time of the observation, respectively (they coincide for the Main Alfvén Wing spot observations). The X, Y and Z System-III coordinates of the spot are reported in column 8, 9 and 10. The last six columns contain the upper (up) and lower (dw) error on the spot position.

Table S16.

Cartesian coordinates in km of the Europa footprint in the southern hemisphere, corresponding to the data points in Figure 1 of the main text. The first column contains the perijove (PJ) number, the second the hemisphere observed. The third, fourth and fifth columns contain the date of the observation, while the sixth and seventh columns are the starting and ending time of the observation, respectively (they coincide for the Main Alfvén Wing spot observations). The X, Y and Z System-III coordinates of the spot are reported in column 8, 9 and 10. The last six columns contain the upper (up) and lower (dw) error on the spot position.

Table S17.

Cartesian coordinates in km of the Ganymede footprint in the northern hemisphere, corresponding to the data points in Figure 1 of the main text. The first column contains the perijove (PJ) number, the second the hemisphere observed. The third, fourth and

fifth columns contain the date of the observation, while the sixth and seventh columns are the starting and ending time of the observation, respectively (they coincide for the Main Alfvén Wing spot observations). The X, Y and Z System-III coordinates of the spot are reported in column 8, 9 and 10. The last six columns contain the upper (up) and lower (dw) error on the spot position.

Table S18.

Cartesian coordinates in km of the Ganymede footprint in the southern hemisphere, corresponding to the data points in Figure 1 of the main text. The first column contains the perijove (PJ) number, the second the hemisphere observed. The third, fourth and fifth columns contain the date of the observation, while the sixth and seventh columns are the starting and ending time of the observation, respectively (they coincide for the Main Alfvén Wing spot observations). The X, Y and Z System-III coordinates of the spot are reported in column 8, 9 and 10. The last six columns contain the upper (up) and lower (dw) error on the spot position.

Table S19.

Cartesian coordinates in km of the Io footprint tail in the northern hemisphere, corresponding to the data points in Figure 1 of the main text. The first column contains the perijove (PJ) number, the second the hemisphere observed. The third, fourth and fifth columns contain the date of the observation, while the sixth and seventh columns are the starting and ending time of the observation, respectively. The X, Y and Z System-III coordinates of the tail are reported in column 8, 9 and 10. The last six columns contain the upper (up) and lower (dw) error on the tail position.

Table S20.

Cartesian coordinates in km of the Io footprint tail in the southern hemisphere, corresponding to the data points in Figure 1 of the main text. The first column contains the perijove (PJ) number, the second the hemisphere observed. The third, fourth and fifth columns contain the date of the observation, while the sixth and seventh columns are the starting and ending time of the observation, respectively. The X, Y and Z System-III coordinates of the tail are reported in column 8, 9 and 10. The last six columns contain the upper (up) and lower (dw) error on the tail position.

Table S21.

Cartesian coordinates in km of the Europa footprint tail in the northern hemisphere, corresponding to the data points in Figure 1 of the main text. The first column contains the perijove (PJ) number, the second the hemisphere observed. The third, fourth and fifth columns contain the date of the observation, while the sixth and seventh columns are the starting and ending time of the observation, respectively. The X, Y and Z System-III coordinates of the tail are reported in column 8, 9 and 10. The last six columns contain the upper (up) and lower (dw) error on the tail position.

Table S22.

Cartesian coordinates in km of the Europa footprint tail in the southern hemisphere, corresponding to the data points in Figure 1 of the main text. The first column contains the perijove (PJ) number, the second the hemisphere observed. The third, fourth and fifth columns contain the date of the observation, while the sixth and seventh columns are the starting and ending time of the observation, respectively. The X, Y and Z System-III coordinates of the tail are reported in column 8, 9 and 10. The last six columns contain the upper (up) and lower (dw) error on the tail position.

Table S23.

Cartesian coordinates in km of the Ganymede footprint tail in the northern hemisphere, corresponding to the data points in Figure 1 of the main text. The first column contains the perijove (PJ) number, the second the hemisphere observed. The third, fourth and fifth columns contain the date of the observation, while the sixth and seventh columns are the starting and ending time of the observation, respectively. The X, Y and Z System-III coordinates of the tail are reported in column 8, 9 and 10. The last six columns contain the upper (up) and lower (dw) error on the tail position.

Table S24.

Cartesian coordinates in km of the Ganymede footprint tail in the southern hemisphere, corresponding to the data points in Figure 1 of the main text. The first column contains the perijove (PJ) number, the second the hemisphere observed. The third, fourth and fifth columns contain the date of the observation, while the sixth and seventh columns are the starting and ending time of the observation, respectively. The X, Y and Z System-III coordinates of the tail are reported in column 8, 9 and 10. The last six columns contain the upper (up) and lower (dw) error on the tail position.

References

Acton, C., Bachman, N., Semenov, B., & Wright, E. (2018, January). A look towards the future in the handling of space science mission geometry. *Planetary and Space Science*, *150*, 9–12. doi: 10.1016/j.pss.2017.02.013

Acton, C. H. (1996, January). Ancillary data services of NASA's Navigation and Ancillary Information Facility. *Planetary and Space Science*, *44*(1), 65–70. doi: 10.1016/0032-0633(95)00107-7

Allegrini, F., Gladstone, G. R., Hue, V., Clark, G., Szalay, J. R., Kurth, W. S., ... Wilson, R. J. (2020, September). First Report of Electron Measurements During a Europa Footprint Tail Crossing by Juno. *Geophys. Res. Lett.*, *47*(18). doi: 10.1029/2020GL089732

Sulaiman, A. H., Hospodarsky, G. B., Elliott, S. S., Kurth, W. S., Gurnett, D. A., Imai, M., ... Bolton, S. J. (2020, August). Wave-particle interactions associated with Io's auroral footprint: Evidence of Alfvén, ion cyclotron, and whistler modes. *Geophys. Res. Lett.*. doi: 10.1029/2020GL088432

Szalay, J. R., Allegrini, F., Bagenal, F., Bolton, S. J., Bonfond, B., Clark, G., ... Wilson, R. J. (2020a, February). Alfvénic Acceleration Sustains Ganymede's Footprint Tail Aurora. *Geophys. Res. Lett.*, *47*(3). doi: 10.1029/2019GL086527

Szalay, J. R., Allegrini, F., Bagenal, F., Bolton, S. J., Bonfond, B., Clark, G., ... Wilson, R. J. (2020b, September). A New Framework to Explain Changes in Io's Footprint Tail Electron Fluxes. *Geophys. Res. Lett.*, *47*(18). doi: 10.1029/2020GL089267

Tao, C., Badman, S. V., & Fujimoto, M. (2011, June). UV and IR auroral emission model for the outer planets: Jupiter and Saturn comparison. *Icarus*, *213*(2), 581–592. doi: 10.1016/j.icarus.2011.04.001